Identifying the Molecular Edge Termination of Exfoliated Hexagonal Boron Nitride Nanosheets with Solid-State NMR Spectroscopy and Plane-Wave DFT Calculations

*Rick W. Dorn[1,2], Matthew J. Ryan[2], Tae-Hoon Kim[2], Tian Wei Goh[1,2], Patrick M. Heintz,[1,2] Lin Zhou[1], Wenyu Huang[1,2], Aaron J. Rossini[1,2] **

[1]*US Department of Energy, Ames Laboratory, Ames, Iowa, USA, 50011*

[2]*Iowa State University, Department of Chemistry, Ames, IA, USA, 50011*

AUTHOR INFORMATION

Corresponding Author

*e-mail: arossini@iastate.edu, phone: 515-294-8952.

Keywords: Nuclear Magnetic Resonance, Density-Functional Theory, *h*-BN, White Graphene

TOC

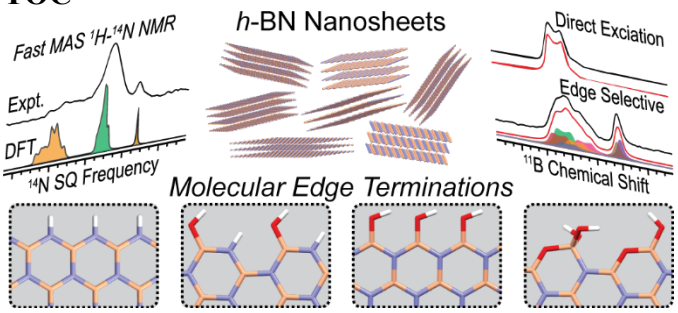

Abstract

Hexagonal boron nitride nanosheets (*h*-BNNS), the isoelectric analog to graphene, have received much attention over the past decade due to their high thermal oxidative resistance, high bandgap, catalytic activity and low cost. The molecular functional groups that terminate boron and nitrogen zigzag and/or armchair edges directly affect their chemical, physical and electronic properties. However, an understanding of the exact molecular edge termination present in *h*-BNNS is lacking. Here, high-resolution magic-angle spinning (MAS) solid-state NMR (SSNMR) spectroscopy and plane-wave density-functional theory (DFT) calculations are used to determine the exact molecular edge termination in exfoliated *h*-BNNS. $^{1}H \rightarrow ^{11}B$ cross-polarization MAS (CPMAS) SSNMR spectra of *h*-BNNS revealed multiple hydroxyl/oxygen coordinate boron edge sites that were not detectable in direct excitation experiments. A dynamic nuclear polarization (DNP)-enhanced $^{1}H \rightarrow ^{15}N$ CPMAS spectrum of *h*-BNNS displayed four distinct ^{15}N resonances while a 2D $^{1}H\{^{14}N\}$ dipolar-HMQC spectrum revealed three distinct ^{14}N environments. Plane-wave DFT calculations were used to construct model edge structures and predict the corresponding ^{11}B, ^{14}N and ^{15}N SSNMR spectra. Comparison of the experimental and predicted SSNMR spectra confirms that zigzag and armchair edges with both amine and boron hydroxide/oxide termination are present. The detailed characterization of *h*-BNNS molecular

edge termination will provide usefulness for many material science applications and the techniques outlined here should be applicable to comprehensively understand the molecular edge terminations in other 2D materials.

Introduction

Atomically thin layered materials are of high importance due to their unique physical, chemical and electronic properties. Since the pioneering work by Novoselov *et. al.* on graphene in 2004,[1] extensive work has emerged on graphene[2-6] and other two-dimensional (2D) materials, such as hexagonal boron nitride (*h*-BN) nanosheets (*h*-BNNS),[7-15] transition metal dichalcogenide nanosheets,[7, 11, 16] borophenes,[17-20] phosphorenes,[21-23] etc. *h*-BN, an isoelectric analog to graphite, can be exfoliated to yield *h*-BNNS in a similar manner as graphene (Scheme 1).[8-9, 24-27] *h*-BNNS, sometimes referred to as white graphene, has received much attention over the past decade due to their high thermal oxidative resistance (ca. 840 ^{o}C),[28] high bandgap (5-6 eV),[8, 25, 29-30] catalytic activity,[31-35] and low cost. Recently, *h*-BN/*h*-BNNS[31, 34-36] and *h*-BN hybrids[37-39] have been shown to be promising metal-free catalysts for a variety of reactions. Notably, *h*-BN was recently shown to be an excellent catalyst for the selective oxidative dehydrogenation (ODH) of propane to propene, a critical feedstock chemical.[31]

A comprehensive understanding of structure-function relationships is required for the rational design and further development of next-generation materials. While the bulk structure of *h*-BN has been known for over a half century from X-ray diffraction (XRD) studies,[40] the exact molecular edge termination of *h*-BN and *h*-BNNS (Scheme 1) is unknown, despite their likely importance for catalysis[31-34] and material science applications.[41-44] Previously, a high-resolution transmission electron microscopy (HRTEM) study of mono-layered *h*-BNNS revealed both zigzag and armchair edge termination of the sheets occurs.[45] However, microscopy images may not be

representative of the ensemble and many edge terminations have been proposed. For example, Lin *et. al.* suggested boron edges terminated with hydroxyl groups are favored as a result from sonication assisted hydrolysis during the aqueous exfoliation process in water.[27] Density-functional theory (DFT) calculations by Lopez-Bezanilla *et. al.* suggested that armchair edges are favorable, with B-OH and N-OH functional groups stabilized through a hydrogen-bonding network.[46] Numerous other computational studies have predicted stable molecular edge structures and the corresponding electronic properties for *h*-BN systems.[42, 47-55] Furthermore, several edge structures have been proposed as catalytically active sites for the selective ODH of alkanes to alkenes.[31-33, 35] Arunachalam *et. al. used* one-dimensional (1D) direct excitation ^{1}H and ^{11}B solid-state NMR (SSNMR) experiments to characterize *h*-BNNS. They suggested that both N-H and B-OH edge termination occurs, however, their 1D NMR spectra do not provide definitive evidence for N-H and B-OH edge terminations.[56] In summary, analysis of the prior literature clearly demonstrates that the exact molecular edge termination of *h*-BN and *h*-BNNS is still unknown.

The molecular structure of the *h*-BNNS edges is likely unknown because common characterization techniques for 2D materials, such as scanning electron microscopy (SEM) or TEM, powder or single-crystal XRD, X-ray photoelectron spectroscopy (XPS) and Raman spectroscopy, often provide only a partial picture of molecular structure. It is often difficult to determine the exact molecular structure of edge/defect sites in 2D materials because they typically exhibit structural disorder and the bulk sites are orders of magnitude higher in concentration. High-resolution magic-angle spinning (MAS) solid-state NMR (SSNMR) spectroscopy is a powerful technique to probe and comprehensively characterize layered materials.[57-63] For example, ^{13}C homonuclear correlation SSNMR experiments of ^{13}C-labeled graphene oxide provide the molecular structure and bonding connectivities between sp^2 carbons

and functional groups present within the material.[64] Polarization transfer techniques, such as cross-polarization (CP), heteronuclear multiple-quantum correlation (HMQC) and insensitive nuclei polarization transfer (INEPT), may be used to selectively detect only edge and/or defect sites within materials, thus allowing for the possibility to determine the exact molecular structure of edge and/or defect sites.[65-69]

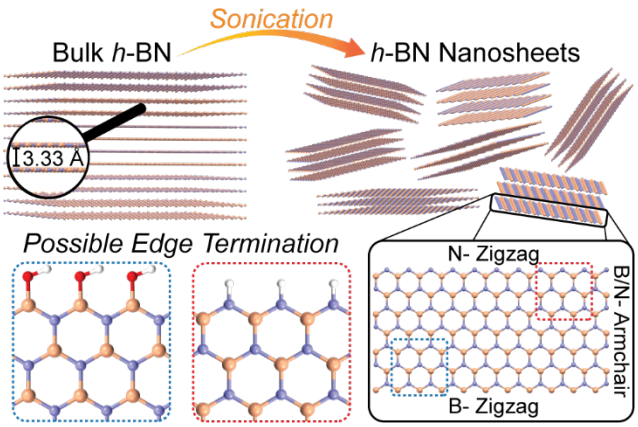

Scheme 1. Illustration for the sonication assisted exfoliation of bulk *h*-BN to *h*-BNNS. The nitrogen (N-) and boron (B-) zigzag and armchair edges are indicated. Two possible zigzag molecular edge terminations are shown.

Here, we use state-of-the-art high-resolution SSNMR spectroscopy, including dynamic nuclear polarization (DNP) and fast magic angle spinning (MAS) heteronuclear correlation experiments, in conjunction with periodic plane-wave density-functional theory (DFT) calculations to probe and determine the exact molecular edge termination in *h*-BNNS. *h*-BNNS were synthesized via sonication assisted exfoliation of *h*-BN in water. Electron microscopy (SEM and TEM) images before (*h*-BN) and after (*h*-BNNS) sonication confirmed the nanosheets were successfully

exfoliated from the bulk material with lateral dimensions between 40 and 250 nm and typical sheets consisting of ca. 10-50 BN layers. Variable temperature diffusive reflectance infrared Fourier transform (DRIFTS) spectroscopy suggested possible molecular functional groups present on the edge of the BN sheets. $^{1}H \rightarrow ^{11}B$ CPMAS SSNMR spectroscopy experiments revealed hydroxyl/oxygen coordinated boron edge sites that were not detectable in direct excitation ^{11}B NMR experiments. DNP-enhanced ^{11}B homonuclear correlation spin-diffusion experiments confirm the proximity of the boron edge sites to that of bulk boron atoms within the BN lattice. DNP-enhanced $^{1}H \rightarrow ^{15}N$ CPMAS experiments at natural isotopic abundance (ca. 0.37 %) revealed four distinct nitrogenenvironments while $^{1}H\{^{14}N\}$ dipolar-HMQC (D-HMQC) experiments indicated three distinct nitrogen environments. Measurement of the ^{1}H-^{14}N dipolar coupling constant unambiguously confirms the presence of N-H edge termination. Finally, periodic plane-wave DFT calculations were performed to build model edge structures and predict ^{11}B, ^{14}N and ^{15}N SSNMR spectra. DFT calculated ^{11}B spectra of model edge termination structures illustrated that increasing hydroxyl/oxygen coordination decreased the ^{11}B isotropic chemical shift (δ_{iso}), lending credence to the assigned boron edge molecular structures. Comparison between the experimental and DFT calculated ^{14}N and ^{15}N NMR spectra confirms that both N-H armchair and zigzag amine edge termination occurs, with the armchair N-H edge termination being the more prevalent amine termination.

Results and Discussion

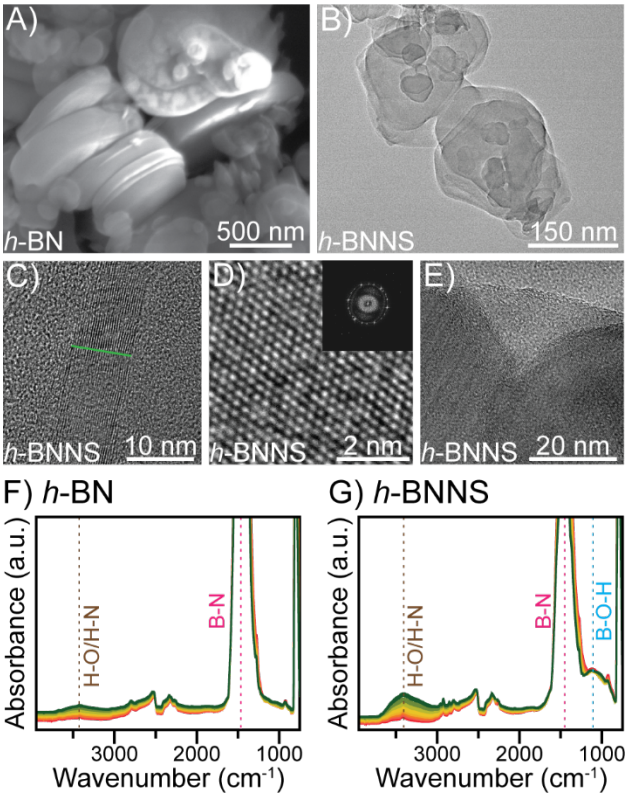

Figure 1. (A) SEM image of *h*-BN showing lateral dimensions and layer thickness. (B-E) TEM images of *h*-BNNS showing (B) lateral dimension, (C) thickness (~ 25 layers), (D) honeycomb lattice and (E) edge sites. (F-G) Variable temperature DRIFTS spectra of (F) *h*-BN and (G) *h*-BNNS ranging from 40 °C (green) to 300 °C (red) under an He atmosphere.

Electron Microscopy. SEM and TEM imaging are frequently used to investigate the exfoliation of bulk materials to atomically thin layered materials.[6, 26, 70-73] Here, we used SEM and TEM to directly image the bulk (*h*-BN) and exfoliated (*h*-BNNS) materials to determine the lateral dimensions, layer thickness and attempted to unravel the edge termination. An SEM image of *h*-BN clearly demonstrates the bulk-like nature of the material with layer thickness up to ca. 300 nm (Figure 1A). Assuming an interlayer spacing equal to 3.33 Å, a thickness of 300 nm corresponds to ca. 900 BN layers (Scheme 1).[40] Analysis of the individual h-BN flakes shows there is a large

distribution of lateral sizes, ranging from ca. 10 nm to 1 μm (Figure 1A). After liquid exfoliation, there are clear changes in the lateral sizes and thickness of the sheets. A low magnification TEM image of *h*-BNNS indicates sheet-like features as the contrast is fairly constant across the image (Figure 1B). By obtaining higher magnification TEM images of the sheets parallel to the plane of the electron beam, we can conclude the thickness ranges from ca. 3-17 nm, corresponding to ca. 10-50 BN layers (interlayer spacing ca. 3.6 Å, Figure S1). The reduced thickness confirms the successful exfoliation of *h*-BN (Figure 1C and S2). It should be noted that the lateral sheet width of *h*-BNNS is ca. 40 to 250 nm, a much smaller size distribution than was observed for *h*-BN (Figure 1B and S3A). Previously, it was suggested that sonication assisted hydrolysis occurs during the exfoliation of *h*-BN in water, leading to smaller lateral sheet dimensions and B-$(OH)_2$ edge terminations.[27] However, it is important to keep in mind that centrifugation is used to isolate the exfoliated nanosheets after sonication, likely favoring a smaller range of lateral dimensions and layer thicknesses.[9, 24] We attempted to obtain high magnification TEM images of the edges of *h*-BNNS to determine whether zigzag and/or armchair termination is present (Figure 1E and Figure S3B). Unfortunately, edge features could not be resolved due to the high amount of disorder at the edges and the stacking of multiple layers.

IR Spectroscopy. To determine the possible functional groups present on the edges of *h*-BN and *h*-BNNS, we performed diffuse reflectance infrared Fourier transform spectroscopy (DRIFTS) at temperatures ranging from 40 °C to 300 °C under a constant flow of He. The DRIFTS spectra of *h*-BN (Figure 1F) and *h*-BNNS (Figure 1G) both exhibit a high-intensity B-N stretch (ca. 1450 cm^{-1}) and a low, broad intensity peak at ca. 3400 cm^{-1}, the stretching frequency region typical of N-H and O-H bonds.[74] A third peak is observed in the DRIFTS spectrum of *h*-BNNS of medium intensity at ca. 1115 cm^{-1}, approximately the same frequency observed for a B-O-H bend in boric

acid.[75-76] Upon heating the sample from 40 °C to 300 °C, only the peak at ca. 3400 cm^{-1} decreased in intensity, indicating the removal of absorbed water and/or edge hydroxyl groups.

In summary, electron microscopy and infrared spectroscopy suggest that *h*-BNNS was successfully exfoliated from the bulk material (*h*-BN) in an aqueous solution (H_2O) and the edges are highly disordered, possibly due to amine, hydroxide and oxide edge functionalization. However, there is still a lack of understanding about the type of edge termination (zigzag and/or armchair) and the molecular edge composition; that is, whether amine, hydroxyl or oxide functional groups are present on the zigzag and/or armchair edges. Therefore, we turn to high-resolution SSNMR spectroscopy and periodic plane-wave DFT calculations to probe and unambiguously determine the possible molecular edge terminations in *h*-BNNS.

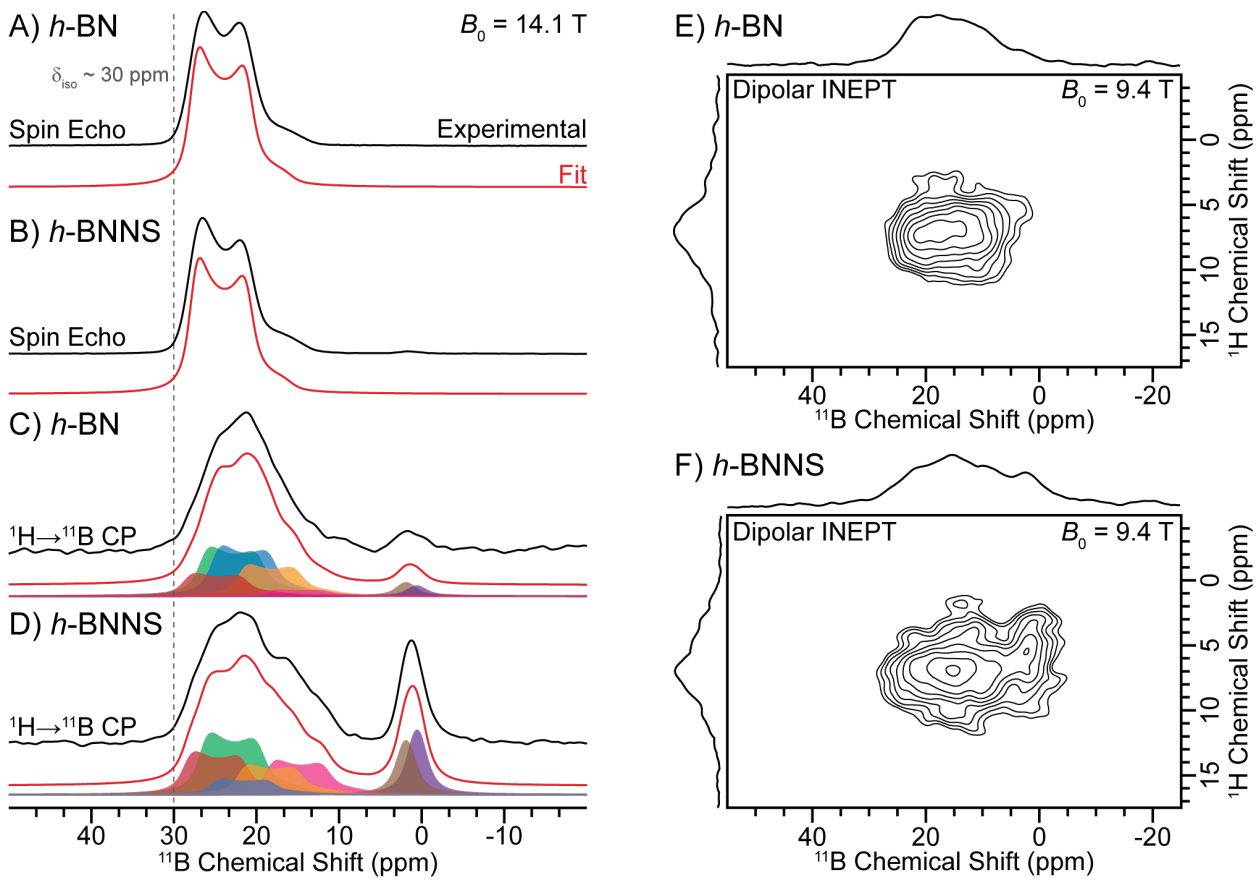

Figure 2: MAS ^{11}B spin echo and ^{1}H→^{11}B cross polarization MAS (CPMAS) NMR spectra of (A, C) *h*-BN and (B, D) *h*-BNNS. The black (top) spectra correspond to the experimental data and the red (bottom) spectra are analytical simulations of central transition quadrupolar powder patterns. The ^{1}H→^{11}B CPMAS NMR spectra were obtained with a 320 µs CP contact time. The dashed gray line indicates δ_{iso}(^{11}B) for the bulk BN_3 ^{11}B signals (spectra A, B and the transparent red fit for C and D). (E, F) 2D ^{1}H→^{11}B dipolar-refocused INEPT (D-RINEPT) spectra of (E) *h*-BN and (F) *h*-BNNS obtained with 480 µs of total $SR4_1^2$ heteronuclear dipolar recoupling. Spectra A-D were acquired at 14.1 T with 25 kHz MAS and spectra E-F were acquired at 9.4 T with 50 kHz MAS.

^{11}B Solid-State NMR Spectroscopy. The molecular edge termination of *h*-BN and *h*-BNNS was first investigated by ^{11}B SSNMR spectroscopy. ^{11}B is an I = 3/2 half-integer quadrupolar nucleus that has a high natural isotopic abundance (ca. 80 %) and a relatively high Larmor frequency

($\nu_0(^{11}B)$ = 128 MHz and $\nu_0(^{1}H)$ = 400 MHz at 9.4 T). ^{11}B isotropic chemical shifts (δ_{iso}) and electric field gradient (EFG) tensor parameters [quadrupolar coupling constant (C_Q) and asymmetry parameter (η)] provide information about the elements and symmetry around the boron nucleus.[77-80] Direct excitation ^{11}B spin echo spectra were recorded for *h*-BN (Figure 2A) and *h*-BNNS (Figure 2B) with 25 kHz MAS at 14.1 T ($\nu_0(^{1}H)$ = 600 MHz). The ^{11}B spin echo SSNMR spectra of both samples display a single quadrupolar powder pattern which is consistent with previously reported ^{11}B SSNMR spectra of bulk *h*-BN[81-83] and corresponds to the boron atoms within the bulk of the sheets (δ_{iso}= 29.5 ppm, C_Q = 2.85 MHz and η = 0.0). The direct excitation ^{11}B spin echo spectra appear to indicate that all boron are trigonal-planar BN_3 in both *h*-BN and *h*-BNNS because only a single site is observed. However, the ^{11}B NMR signals from edge sites will be overwhelmed by the intense ^{11}B NMR signals from bulk-like boron atoms within the BN sheets that correspond to ca. 95-99% of all boron atoms in the sample. Therefore, surface/edge-selective SSNMR techniques are required to resolve additional ^{11}B NMR signals that were previously obscured in the direct excitation spectra. The NMR signals of ^{11}B spins near to the edges can be selectively detected by transferring polarization from ^{1}H spins.[65-69] While recent work has shown that defect sites can be created in the interior of the BN sheets resulting from electron beam irradiation or oxidative etching,[84-88] the TEM images of *h*-BNNS show that the bulk of the sheets are relatively pristine and defect-free, suggesting that ^{1}H spins should mainly be limited to the outer edges (Figure 1D).

Cross polarization (CP) was first used to transfer magnetization from ^{1}H to ^{11}B and selectively detect ^{11}B spins at or near the edge of the BN sheets. The $^{1}H \rightarrow ^{11}B$ CPMAS spectra of *h*-BN (Figure 2C) and *h*-BNNS (Figure 2D) display a relatively featureless broad signal from ca. 7-32 ppm and a sharp signal near 2 ppm. Both ^{11}B CPMAS spectra were fit to seven identical central transition quadrupolar powder pattern sites with varying peak areas (Table 1). The reliability of the peak fits

was confirmed by fitting the edge-selective ^{11}B SSNMR spectra obtained at 9.4 T to identical parameters (δ_{iso}, C_Q, η and peak area, Figure S4).

Simulations suggest that the relatively featureless NMR signal (7-32 ppm) in the $^{1}H \rightarrow ^{11}B$ CPMAS spectra consist of multiple 3-coordinate boron sites with a distribution in their δ_{iso} (ca. 30-20 ppm) and the same C_Q (2.85 MHz) and η (0.0) for each site (Table 1). It is well known that trigonal-planar ^{11}B nuclei typically exhibit a C_Q between 2.5 and 3.0 MHz.[79, 83, 89] Therefore, the simulation suggests that all sites with chemical shifts between 30 and 20 ppm possess trigonal-planar symmetry. The ^{11}B signal that resonates at the highest observed frequency (δ_{iso} = 30.2 ppm, red fit) is similar to the direct excitation ^{11}B spin echo spectrum, suggesting this site corresponds to bulk-like BN_3 sites near to the edge of the sheets. The other trigonal-planar ^{11}B signals observed in the $^{1}H \rightarrow ^{11}B$ CPMAS spectra show a lower $\delta_{iso}(^{11}B)$ compared to the BN_3 sites. Based upon literature ^{11}B chemical shifts,[79, 83, 89] it is known that $\delta_{iso}(^{11}B)$ is reduced when oxygen atoms or hydroxide groups substitute for nitrogen atoms around trigonal-planar boron sites. Therefore, ^{11}B NMR signals with a δ_{iso} of 27-28 ppm (blue and green fits) likely arise from edge sites with a single OH group (trigonal-planar $BN_2(OH)$), while sites with lower δ_{iso} between 20-24 ppm (pink and orange fits) likely result from edge sites with two hydroxyl groups or one hydroxyl group and one bridging oxygen atom (trigonal-planar $BN(OH)_2$ or BNO(OH) sites). The sharp, well-resolved signals with an δ_{iso} of 1.2 ppm (brown fit) and 2.6 ppm (purple fit) correspond to four-coordinate boron environments, likely coordinated by nitrogen and multiple hydroxyl groups/bridging oxygen atoms.[79, 90-92] The relatively small C_Q of 1 MHz and low chemical shift confirms there is tetrahedral symmetry at these boron sites. All of the ^{11}B spectral fits and peak assignments are validated by periodic plane-wave DFT calculations (see below). It is worth noting that the relative ^{11}B peak areas observed in the $^{1}H \rightarrow ^{11}B$ CPMAS spectrum of *h*-BNNS is nearly constant across the

distribution in the $\delta_{iso}(^{11}B)$, while for the bulk material (*h*-BN) the higher frequency signals are much more abundant than the lower frequency signals (Table 1, Figure S5). This suggests that additional oxidation/hydrolysis of the edges occurs during the sonication process in an aqueous solution used to exfoliate the BN layers.

Table 1: Relative peak areas for the fitted $^{1}H \rightarrow ^{11}B$ CPMAS spectra of *h*-BN and *h*-BNNS[a]

δ_{iso} (ppm)	Relative Peak Population for *h*-BN (%)	Relative Peak Population for *h*-BNNS (%)
30.2[b]	13.4	18.5
28.3[b]	29.1	26.7
26.8[b]	29.8	6.8
23.6[b]	18.6	13.0
20.3[b]	3.6	14.8
2.6[c]	3.1	9.2
1.2[c]	2.4	11.0

[a]*h*-BN and *h*-BNNS $^{1}H \rightarrow ^{11}B$ CPMAS spectra were fit to the exact same parameter. [b]C_Q = 2.85 MHz and η = 0.0. [c]C_Q = 1.0 MHz and η = 0.0.

In order to observe the ^{1}H chemical shifts associated with the boron terminated edges, we recorded two-dimensional (2D) $^{1}H \rightarrow ^{11}B$ dipolar-refocused INEPT (D-RINEPT)[93-94] heteronuclear correlation (HETCOR) spectra for *h*-BN and *h*-BNNS at 9.4 T with 50 kHz MAS (Figure 2E and 2F). The ^{1}H SSNMR spin echo spectrum of *h*-BNNS was previously reported and it was suggested that the higher frequency ^{1}H signals (ca. 8 ppm) corresponded to hydroxyl groups on the edges of the BN sheets.[56] However, this assignment was only justified by noting that the ^{1}H NMR signal of boric acid resonates at ca. 8.8 ppm (Figure S6). Here we obtained 2D $^{1}H \rightarrow ^{11}B$ D-RINEPT NMR spectra with a short duration of $SR4_1^2$ heteronuclear dipolar recoupling (480 μs in total) to directly observe ^{1}H spins in close proximity to boron atoms. The 2D $^{1}H \rightarrow ^{11}B$ D-RINEPT spectra of *h*-BN and *h*-BNNS exhibit ^{11}B correlations to broad ^{1}H signals spanning a frequency from ca. 1-12 ppm with maximum signal correlation occurring at ca. 5.5 ppm and 7 ppm for the four- and three-coordinate boron sites, respectively.

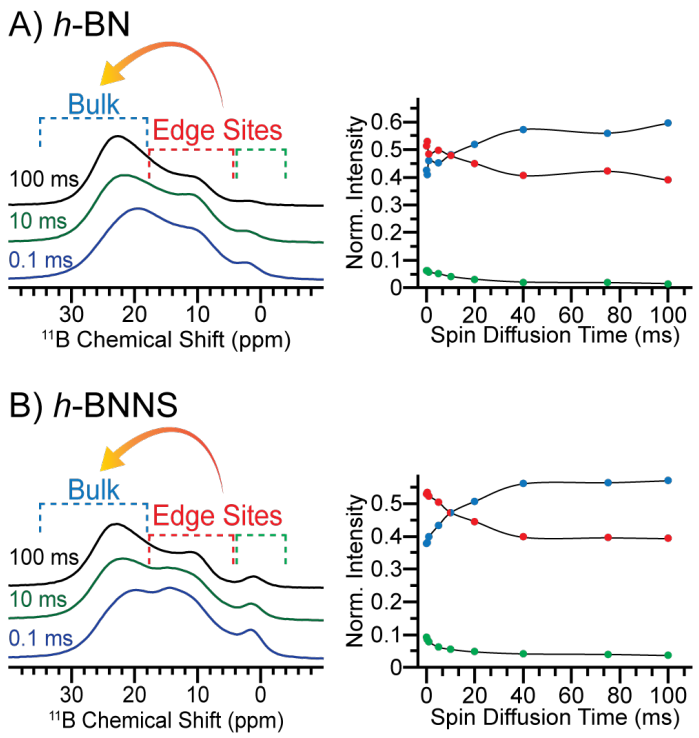

Figure 3: DNP-enhanced 1D $^{1}H \rightarrow ^{11}B$ CP ^{11}B spin-diffusion spectra of (A) *h*-BN and (B) *h*-BNNS. All spectra were acquired on a 400 MHz/263 GHz DNP spectrometer with 10 kHz MAS and a sample temperature of ca. 100 K. Three ^{11}B spin-diffusion spectra are shown for simplicity (left) and the corresponding curves (right) show all spin diffusion points ranging from 0.1 ms to 100 ms (Figure S7). The blue, red and green dots represent bulk (BN_3), 3-coordinate edge and 4-coordinate edge, respectively. The black line does not represent any significance but is used as a guide for the reader. The blue, red and green dashed regions overlaid on the 1D spectra indicate the regions of integration used to construct the spin-diffusion curves.

Edge selective 1D ^{11}B spin-diffusion SSNMR experiments were performed to confirm that the ^{11}B NMR signals in the edge selective SSNMR experiments originate from boron atoms residing on the edge of the BN sheets and are not from residual precursors or impurity phases. It has previously been demonstrated that ^{11}B spin-diffusion readily occurs between ^{11}B spins within organic and inorganic boron compounds.[80, 95] In ^{11}B spin-diffusion experiments, the ^{11}B NMR signals are measured as a function of the ^{11}B spin-diffusion period. The rate at which spin-diffusion

occurs is primarily determined by the distance (dipolar coupling constant) between the two spins.[95-97] Dynamic nuclear polarization surface-enhanced NMR spectroscopy (DNP SENS)[68, 98-101] was used to enhance the sensitivity of the edge selective NMR signals, allowing the ^{11}B spin-diffusion experiments to be performed in just minutes. The *h*-BN and *h*-BNNS samples were prepared for DNP by impregnating them with a TEKPol tetrachloroethane solution.[68, 102] High ^{1}H DNP enhancements (ε_H) above 200 were observed for *h*-BN and *h*-BNNS, consistent with prior observations that boron nitride materials give high proton DNP enhancements (Figure S8).[83, 103] Eight 1D ^{11}B spin-diffusion SSNMR spectra were recorded for both *h*-BN (Figure 3A) and *h*-BNNS (Figure 3B) with varying ^{11}B spin-diffusion times from 100 μs to 100 ms. As the ^{11}B spin-diffusion period increases, there is a clear transfer of signal intensity from the edge ^{11}B NMR signals to bulk-like ^{11}B NMR signals, indicating ^{11}B spin-diffusion from edge site boron atoms to bulk-like boron atoms occurs rapidly. Importantly, the ^{11}B spin-diffusion experiments confirm that the assigned edge signals are not from phase-separated precursors or impurities.

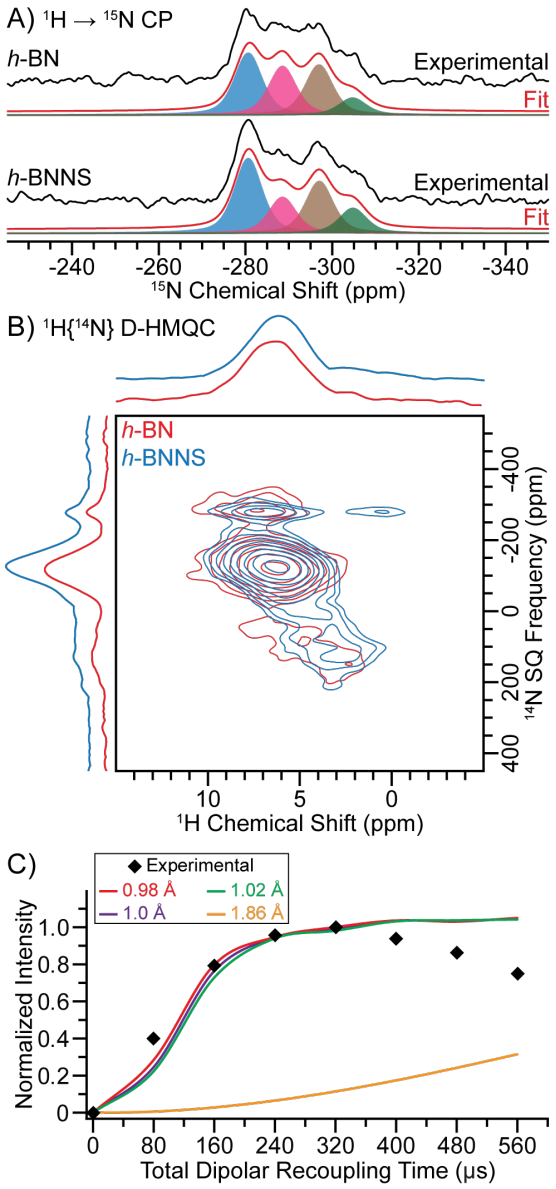

Figure 4: (A) DNP-enhanced $^{1}H \rightarrow ^{15}N$ CPMAS spectra of (top) *h*-BN and (bottom) *h*-BNNS recorded at natural isotopic abundance and with a 5 ms CP contact time. Both spectra were acquired on a 400 MHz/263 GHz DNP spectrometer with 10 kHz MAS and a sample temperature of ca. 100 K. (B) 2D $^{1}H\{^{14}N\}$ dipolar-HMQC (D-HMQC) spectra of (red) *h*-BN and (blue) *h*-BNNS acquired at 9.4 T with 50 kHz MAS. Both spectra were acquired with 400 μs of total $SR4_1^2$ heteronuclear dipolar recoupling. (C) ^{1}H-^{14}N dipolar recoupling build-up curve of (black diamonds) *h*-BNNS (^{1}H peak at ~ 7 ppm) and numerically simulated (SIMPSON)[104] curves for corresponding N-H distances of (red) 0.98 Å, (purple) 1.0 Å, (green) 1.02 Å and (orange) 1.82 Å (resembling an N-OH group).

^{15}N and ^{14}N Solid-State NMR Spectroscopy. ^{14}N and ^{15}N SSNMR spectroscopy was used to determine the exact nitrogen molecular edge termination present in *h*-BN and *h*-BNNS. Nitrogen has two NMR active nuclei, ^{14}N and ^{15}N, with ^{15}N being preferred because it is an $I = 1/2$ nucleus whereas ^{14}N is an $I = 1$ quadrupolar nucleus. However, the low natural isotopic abundance of ^{15}N (ca. 0.37 %) would normally necessitate ^{15}N-labelling to perform edge selective ^{15}N SSNMR experiments. However, natural isotopic abundance ^{15}N SSNMR spectra could be recorded with DNP SENS. The DNP-enhanced ^{1}H → ^{15}N CPMAS spectra of *h*-BN (top) and *h*-BNNS (bottom) were obtained in more than 12 hours each, despite the fact that the ^{1}H DNP enhancements were above 200 for each sample; without the sensitivity gains provided by DNP these experiments would have required over 20 years of signal averaging for each sample. The ^{15}N CPMAS spectra were acquired with a 5 ms CP contact time to observe ^{15}N signals from bulk-like nitrogen sites (trigonal-planar NB_3) in addition to edge terminated ^{15}N sites. The ^{15}N SSNMR spectra are ca. 40 ppm broad and can be fit to four distinct nitrogen sites (Figure 4, Table S1, chemical shifts referenced to nitromethane).

To the best of our knowledge there have been four reported nitrogen SSNMR spectra of *h*-BN: (i) a direct excitation ^{14}N spectrum (δ_{iso} = –318 ppm),[105-106] (ii) a direct excitation ^{15}N spectrum (δ_{iso} = –282 ppm, ca. 10 % ^{15}N enrichment),[107] (iii) a ^{1}H→^{15}N CPMAS spectrum (δ_{iso} = –282 ppm and –305 ppm, ca. 10 % ^{15}N enrichment)[107] and (iv) a ^{11}B→^{15}N CPMAS spectrum (δ_{iso} = –320 ppm, recorded at natural isotopic abundance).[106] The δ_{iso}(^{15}N) reported in the previously acquired ^{1}H→^{15}N CPMAS spectrum of *h*-BN matches that observed in our ^{1}H→^{15}N CPMAS spectra of *h*-BN and *h*-BNNS, where they attributed the higher frequency signal (~ –282 ppm) to NB_3 and the lower frequency signal (~ –305 ppm) to NB_2H.[107] In addition, ^{15}N SSNMR

spectroscopy experiments on borazine-based compounds containing trigonal-planar NB_3 and NB_2H groups revealed that NB_3 environments typically show $\delta_{iso}(^{15}N)$ between ca. –257 and –286 ppm and NB_2H environments typically show $\delta_{iso}(^{15}N)$ between ca. –284 and –313 ppm.[108-110] Furthermore, previous *ab initio* ^{15}N chemical shift calculations of hydrogen-saturated α-BN clusters suggest that a NB_3 site within the BN lattice has a predicted $\delta_{iso}(^{15}N) = -285$ ppm and a NB_2H group residing on the edge of the BN sheet has a predicted $\delta_{iso}(^{15}N) = -305$ ppm.[111] Therefore, we initially suggest that the two higher frequency ^{15}N signals correspond to bulk NB_3 sites near the edge of the BN sheet ($\delta_{iso} \sim -280$ ppm and –288 ppm, blue and pink fits, respectively). The two lower frequency ^{15}N signals correspond to NB_2H groups residing on zigzag or armchair edges ($\delta_{iso} \sim -297$ ppm and –305 ppm, brown and green fits, respectively).

We next turn to fast MAS (ν_{rot} = 50 kHz) ^{14}N SSNMR spectroscopy. ^{14}N is appealing for SSNMR spectroscopy because of its high natural isotopic abundance (ca. 99.6%). Fast MAS $^{1}H\{^{14}N\}$ heteronuclear multiple-quantum correlation (HMQC) experiments are often used to indirectly detect ^{14}N solid-state NMR spectra with high sensitivity.[112-114] The 2D $^{1}H\{^{14}N\}$ dipolar-HMQC (D-HMQC) SSNMR spectra of *h*-BN (Figure 4B, red) and *h*-BNNS (Figure 4B, blue) both reveal three distinct ^{14}N signals at ca. –275 ppm, –125 ppm and 100 ppm. Since ^{14}N is an $I = 1$ quadrupolar nucleus, the observed peak position is determined by both the $\delta_{iso}(^{14}N/^{15}N)$ and the quadrupolar induced shift (QIS), which is related to the symmetry at the nitrogen nucleus (the QIS is proportional to the square of the C_Q). The peak-width is mainly determined by the second-order quadrupolar interaction and is therefore also proportional to the square of C_Q.

It has been previously reported that bulk NB_3 sites in *h*-BN exhibit spherical symmetry (C_Q = 140 kHz),[106] indicating that NB_3 ^{14}N and ^{15}N signals will be observed at ca. the same peak position determined by the δ_{iso} because the QIS is negligible for low C_Q sites. Therefore, the sharp,

low intensity ^{14}N NMR signal at ca. –275 ppm is assignted to NB_3 sites near the edge of the BN sheet. The two higher frequency, more intense ^{14}N NMR signals experience additional spectral broadening and a substantial QIS due to a significant ^{14}N quadrupolar interaction ($C_Q > 1$ MHz). The observation of a significant C_Q suggests the edge termination is such that the local symmetry around the ^{14}N nucleus is distorted. The most intense ^{14}N NMR signal (~ –125 ppm) illustrates strong correlations to ^{1}H spins at ca. 6 ppm while the highest frequency ^{14}N NMR signal (~ 100 ppm) is correlated to ^{1}H spins at ca. 3 ppm. Previously, Arunachalam *et. al.* reported that the N-H ^{1}H NMR signal of *h*-BNNS resonates at 1.6 ppm, in contradiction with the results presented here.[56] However, their peak assignment had no experimental basis.

To confirm the presence of covalently bonded N-H groups on the edge of the BN sheets as previous literature seems to suggest, a $^{1}H\{^{14}N\}$ dipolar-HMQC signal build-up curve was recorded to estimate the ^{1}H-^{14}N heteronuclear dipolar coupling constant and corresponding inter-nuclear distance (Figure 4C). The dipolar coupling constant between to spins (D_{ij}) is inversely proportional to the inter-nuclear distance cubed ($D_{ij} \propto r_{ij}^{-3}$) and the rate at which coherence is generated is directly related to the dipolar coupling constant. Therefore, by comparing the experimental dipolar recoupling build-up curve for *h*-BNNS (black diamonds) to that of numerically simulated curves (SIMPSON)[104] for different N-H bond distances, we can clearly see that the two most intense ^{14}N signals correspond to NB_2H groups residing on the edge of the BN sheet. It is worth mentioning that the experimental dipolar recoupling build-up curve deviates from the numerical simulations at long recoupling times. The deviation of the experimental curve is most likely due to three parameters: (i) the effective refocused transverse relaxation constant (T_2') under heteronuclear dipolar recoupling, (ii) different ^{14}N C_Q for the two sites and (iii) an extensive ^{1}H-^{14}N dipolar coupling network from B-OH edges and bulk nitrogen atoms within the lattice (see Supporting

Information for more discussion). Nevertheless, the ^{14}N and ^{15}N SSNMR experiments confirm there are two distinct NB_2H edge sites present in *h*-BN and *h*-BNNS. Below, plane-wave DFT calculations are used to create structural models of the edge terminations and predicted ^{1}H, ^{11}B, ^{14}N and ^{15}N NMR spectra are compared to the corresponding experimental spectra.

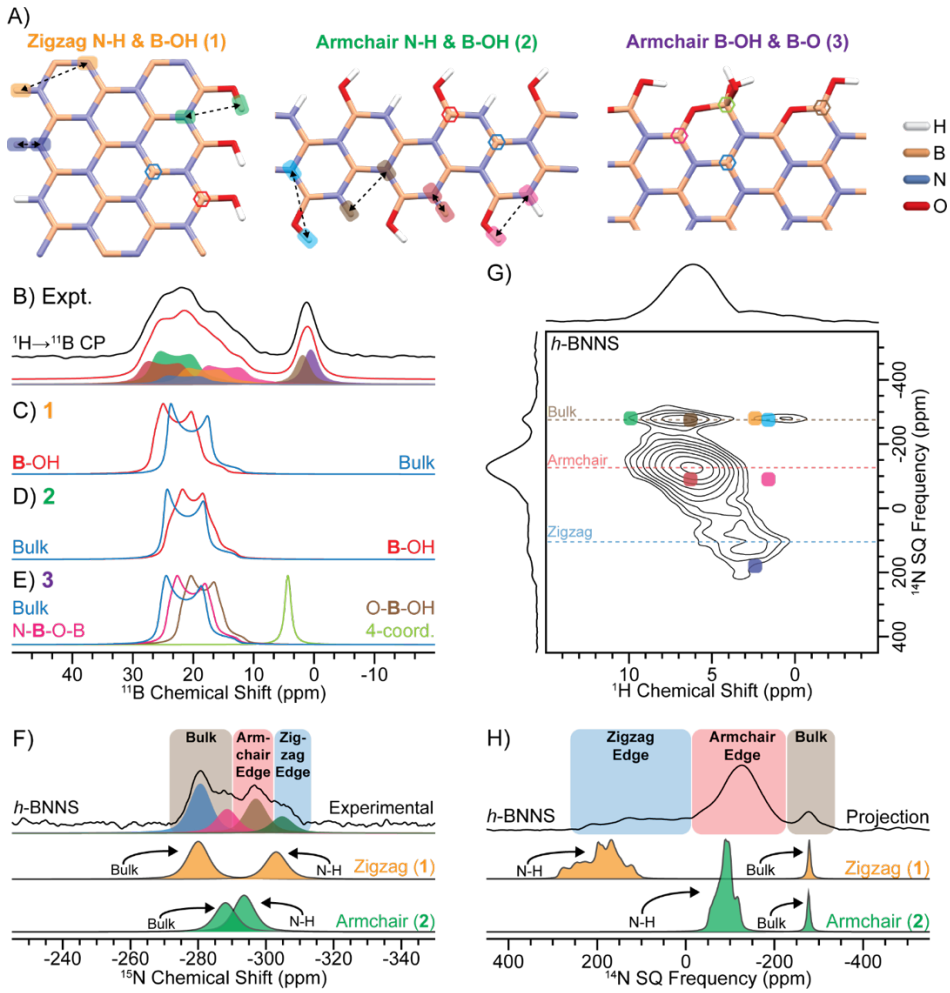

Figure 5: Plane-wave DFT calculated edge structures and NMR parameters. (A) Three structural models of zigzag edges with N-H and B-OH termination (**1**, orange), armchair edges with N-H and B-OH termination (**2**, green) and armchair edges with B-OH and B-O termination (**3**, purple). The unfilled hexagons correspond to ^{11}B predict chemical shifts in B-E and the filled rectangles correspond to ^{1}H and ^{14}N predicted chemical shifts and SQ frequencies in G. (B-E) Comparison of the experimental (B) ^{11}B CPMAS spectrum of *h*-BNNS from Figure 2 and the predicted ^{11}B spectra from models (C) **1**, (D) **2** and (E) **3**. (F) Comparison of the (black, top) experimental DNP-enhanced ^{1}H→^{15}N CPMAS spectrum of *h*-BNNS and predicted ^{15}N NMR spectra for model **1** (orange) and model **2** (green, bottom). (G) Experimental ^{1}H{^{14}N} D-HMQC spectrum of *h*-BNNS from Figure 4 overlaid with predicted ^{1}H chemical shifts and ^{14}N SQ NMR spectra for model **1** and model **2**. (H) Comparison of the (black, top) experimental ^{14}N projection of *h*-BNNS and simulated spectra for (orange, middle) **1** and (green, bottom) **2**.

Plane-Wave DFT Calculations. Plane-wave DFT calculations of NMR parameters (chemical shielding tensors, EFG tensors and scalar (*J*-) couplings) using the gauge including projected augmented wave (GIPAW)[115] approach are frequently applied to aid in the interpretation and deconvolution of SSNMR spectra for organic and inorganic solids.[116-125] Here, we utilize periodic plane-wave DFT calculations using the GIPAW approach[115] as implemented in CASTEP[126] to build structural models of *h*-BNNS edge termination and calculate ^{1}H, ^{11}B and ^{14}N/^{15}N chemical shifts and ^{11}B and ^{14}N EFG tensors. Three structural edge termination models were constructed based upon the experimental SSNMR data discussed above and the previous hypothesis that *h*-BNNS possesses both zigzag and armchair edge termination (Figure 5A).[45] The three structural models possess the following molecular edge terminations: (**1**) zigzag edge with NB_2H and $BN_2(OH)$ termination, (**2**) armchair edge with NB_2H and $BN_2(OH)$ termination and (**3**) armchair edge with BN_2O, BNO(OH) and $BNO(OH)_2$.

First, the plane-wave DFT calculated $\delta_{iso}(^{11}B)$ and EFG tensors for models **1**, **2** and **3** are compared with the experimental $^{1}H \rightarrow ^{11}B$ CPMAS spectrum of *h*-BNNS (Figure 5B-E). The exact calculated $\delta_{iso}(^{11}B)$ and EFG tensors for **1**, **2** and **3** are given in Table S3. The calculated ^{11}B NMR spectra of **1** (zigzag NB_2H and $BN_2(OH)$) and **2** (armchair NB_2H and $BN_2(OH)$) reveal two distinct boron sites corresponding to bulk (BN_3, blue) and edge ($BN_2(OH)$, red) boron atoms. There is only a slight difference in the calculated $\delta_{iso}(^{11}B)$ for the two sites, with the edge site ($BN_2(OH)$) exhibiting a higher predicted $\delta_{iso}(^{11}B)$ for the zigzag edge termination (**1**) and a lower predicted $\delta_{iso}(^{11}B)$ for the armchair edge termination (**2**) when compared to the bulk sites (BN_3). As mentioned above, we hypothesized that the $\delta_{iso}(^{11}B)$ only decreases by ca. 2-3 ppm for an $BN_2(OH)$ edge compared to BN_3 within the BN lattice. The plane-wave DFT calculations are not expected to accurately differentiate the slight difference in the $\delta_{iso}(^{11}B)$ for $BN_2(OH)$ and BN_3 sites as the

chemical shielding to chemical shift calibration curve indicates a relative uncertainty of ca. 2 ppm (Figure S12A, Table S4). The DFT calculated ^{11}B spectrum of **3** (armchair B-OH and B-O) exhibits four distinct boron sites due to BN_3 (blue), BN_2O (pink), BNO(OH) (brown) and $BNO(OH)_2$ (green, four-coordinate) environments. The predicted $\delta_{iso}(^{11}B)$ decreases with increasing O/OH coordination, giving credence to our previous assignment above. The DFT calculated peak position (δ_{iso} = 4.7 ppm) and C_Q (0.7 MHz) for the four-coordinate site ($BNO(OH)_2$) matches the experimentally observed 4-coordinate boron site well, further suggesting this edge termination is present in *h*-BN and *h*-BNNS.

We next turn to the calculated $\delta_{iso}(^{15}N)$ for the zigzag (**1**) and armchair (**2**) NB_2H edge termination models and compare that with the experimental $^{1}H\rightarrow^{15}N$ CPMAS spectrum of *h*-BNNS (Figure 5F, Table S5). The predicted ^{15}N NMR spectra of **1** (zigzag, orange) and **2** (armchair, green) display excellent agreement with the experimental $^{1}H\rightarrow^{15}N$ CPMAS spectra of *h*-BN and *h*-BNNS (calculated δ_{iso} within ca. 3.5 ppm of experimental δ_{iso}). Both **1** and **2** exhibit two distinct ^{15}N environments corresponding to NB_3 (bulk) and NB_2H (edge), where the bulk site exhibits a higher calculated $\delta_{iso}(^{15}N)$ and the edge site exhibits a lower calculated $\delta_{iso}(^{15}N)$, in agreement with previous literature.[107-111] The individual NB_3 and NB_2H sites for the different edge terminations (zigzag and armchair) also exhibit slightly different predicted $\delta_{iso}(^{15}N)$, where the NB_3 site for the zigzag edge termination (**1**, −280.0 ppm) is predicted to have a higher calculated $\delta_{iso}(^{15}N)$ than the armchair NB_3 site (**2**, −288.8 ppm) and the zigzag NB_2H site (**1**, −303.7 ppm) is predicted to have a lower calculated $\delta_{iso}(^{15}N)$ than the armchair NB_2H site (**2**, −293.4 ppm). Notably, the plane-wave DFT calculations predict that the ^{15}N signals for zigzag (**1**) and armchair (**2**) NB_2H edge terminations can be clearly resolved, allowing us to suggest that both zigzag and armchair NB_2H edge termination occurs.

Comparison of the DFT calculated $\delta_{iso}(^{14}N)$ and EFG tensors (C_Q and η) with the 2D $^{1}H\{^{14}N\}$ D-HMQC ^{14}N SQ frequency projection of *h*-BNNS unambiguously shows that both NB_2H armchair (green, **2**) and zigzag (orange, **1**) edge terminations are present as the armchair and zigzag NB_2H ^{14}N signals are clearly resolved (Figure 5H). Here, the QIS for ^{14}N offers enhanced resolution compared to ^{15}N because the NB_2H armchair and zigzag nitrogen atoms have a different C_Q (DFT calc. = 1.4 MHz and 2.2 MHz, respectively). Furthermore, comparison of the relative peak intensities for the zigzag and armchair edge termination illustrates that the armchair NB_2H edge termination is the most prevalent, consistent with the relative peak intensities obtained from the $^{1}H\rightarrow^{15}N$ CPMAS spectrum of *h*-BNNS (Figure 5F). For both zigzag (**1**) and armchair (**2**) NB_2H edge termination models, the predicted ^{1}H and ^{14}N peak positions show reasonable overlap with the experimental 2D $^{1}H\{^{14}N\}$ D-HMQC spectrum (Figure 5G), corroborating all of the previous peak assignments.

Conclusions

In summary, the exact molecular edge termination of *h*-BN and *h*-BNNS was identified by high-resolution MAS SSNMR spectroscopy and plane-wave DFT calculations. $^{1}H\rightarrow^{11}B$ CPMAS SSNMR experiments revealed multiple hydroxyl/oxygen coordinated boron edge sites (three and four-coordinate boron) that are not detected in direct excitation ^{11}B SSNMR experiments. 1D DNP-enhanced edge-selective ^{11}B spin-diffusion experiments confirm the boron edge sites observed in the $^{1}H\rightarrow^{11}B$ CPMAS spectra reside on the edge on the BN sheet and are not from residual precursors or impurity phases. DNP-enhanced $^{1}H\rightarrow^{15}N$ CPMAS spectra revealed four distinct ^{15}N environments and 2D $^{1}H\{^{14}N\}$ D-HMQC spectra revealed three distinct ^{14}N environments. Finally, periodic plane-wave DFT calculations were used to build edge structural

models and predict ^{11}B, ^{14}N and ^{15}N SSNMR spectra. The DFT calculated ^{11}B SSNMR spectra for zigzag/armchair edge termination containing BN_2O, $BN_2(OH)$, BNO(OH) and $BNO(OH)_2$ edge functional groups illustrated that the $\delta_{iso}(^{11}B)$ decreases as the hydroxyl/oxygen coordination increases, explaining the appearance of the $^{1}H \rightarrow ^{11}B$ CPMAS spectra. Comparison of the experimental and DFT calculated ^{14}N and ^{15}N NMR spectra confirm that both N-H armchair and zigzag edge termination occurs with the N-H armchair edge termination being the more prevalent of the two. The comprehensive structural characterization of *h*-BNNS edge termination will aid the development of this extensively studied material. Furthermore, the techniques outlined here should provide a detailed strategy to characterize edge/defect sites in other atomically thin-layered materials of interest.

Methods

Bulk h-BN Exfoliation. The exfoliation of *h*-BN to *h*-BNNS was modified from previous literature.[56] To summarize, 1 g of *h*-BN (nanopowder, SkySpring Nanomaterials, Inc.) was dispersed in 500 mL of DI H_2O. The *h*-BN dispersion was sonicated for ca. 4.5 hours (1 second/5 second on/off duty cycle) using a 500 W tip sonicator at 50 % amplitude. To avoid sample heating, the aqueous solution was cooled by submerging ca. 1/3 of the beaker containing the *h*-BN dispersion in an ice bath. After ca. 4.5 hours of total sonication (total time including delays ca. 27 hours), the dispersion was allowed to settle at room temperature overnight. Isolated *h*-BNNS were obtained by centrifuging the dispersion at 4500 RPM for 45 min, followed by removing the top 2/3 of the supernatant. Powdered h-BNNS was then obtained by drying the supernatant at 60 ^{o}C for 24 hours.

Electron Microscopy. *h*-BN and *h*-BNNS were suspended in ethanol, then dispersed onto transmission electron microscope grids that have ultrathin carbon film (less than 3 nm) supported by a lacey carbon film on copper mesh (Ted Pella, Inc). The TEM grids were observed by Teneo SEM (Thermo Fisher Scientific) at an acceleration voltage of 20 kV. TEM characterization was performed on a Titan Themis TEM (Thermo Fisher Scientific) at 200 kV.

Diffuse Reflectance Infrared Fourier Transform Spectroscopy. The diffuse reflectance infrared Fourier transform spectroscopy (DRIFTS) spectra were collected using an Agilent Cary 670 FTIR equipped with a linearized Mercury-Cadmium-Telluride (MCT) detector, a Harrick diffuse reflectance accessory, and a Praying Mantis high-temperature reaction chamber. About 20 mg of the powder sample is packed into the IR sample holder equipped with KBr windows. All spectra were obtained at a resolution of 2 cm^{-1} from 700 – 4000 cm^{-1} under atmospheric pressure. The sample was heated to 300 °C in a dynamic He flow (40 mL/min) to remove any adsorbed species from the sample surface. The IR spectra were collected continuously at variable temperatures under a constant 40 mL/min He flow. All sample spectra are subtracted against KBr as the background.

Solid-State NMR Spectroscopy: SSNMR experiments were performed on either a 9.4 T ($\nu_0(^1H)$ = 400 MHz) or 14.1 T ($\nu_0(^1H)$ = 600 MHz) Bruker wide-bore magnet spectrometer equipped with a Bruker Avance III HD or Bruker Avance II consoles, respectively. SSNMR experiments conducted at 9.4 T and 14.1 T were performed using a Bruker 1.3 mm HX MAS and 2.5 mm HXY MAS probe, respectively. In order to tune the 1.3 mm HX MAS probe to ^{14}N ($\nu_0(^{14}N)$ = 28.9 MHz), a 20 pF shunt capacitor was inserted in parallel to the X-channel variable tuning capacitor. The magnetic field strengths were calibrated using ^1H chemical shifts referenced to neat tetramethylsilane with adamantane ($\delta(^1H)$ = 1.82 ppm) as a secondary chemical shift

reference. Previously reported relative NMR frequencies were used to indirectly reference ^{11}B and ^{14}N chemical shifts.[127] Bruker Topspin 3.6.0 was used to process the NMR spectra.

All experimental parameters (MAS frequencies, number of scans, t_1 TD points, t_1 dwell (Δt_1), t_1 acquisition times, CP/dipolar recoupling durations and total experiment acquisition times) are given in Table S6. Longitudinal relaxation (T_1) measurements were performed for ^{1}H and ^{11}B using a saturation recovery experiment. All experiments were performed with recycle delays of $1.3 \times T_1$ unless noted otherwise. ^{1}H radio frequency (RF) pulses were directly calibrated on each sample. All ^{1}H $\pi/2$ RF pulse lengths were 2.5 μs (100 kHz RF field) in duration. Low-power, central transition selective ^{11}B $\pi/2$ RF pulses were 5.0 μs and 7.5 μs in duration for spectra acquired at 9.4 T (1.3 mm HX probe) and 14.1 T (2.5 mm HXY probe), respectively. Rotor assisted population transfer (RAPT) was used to enhance the sensitivity of the direct excitation ^{11}B NMR spectra of *h*-BN and *h*-BNNS acquired at 14.1 T (Figure 1A and 1C).[128-129] 20 μs ^{14}N excitation pulses (1 rotor period with 50 kHz MAS) were used in the ^{1}H{^{14}N} D-HMQC experiments. 25 kHz of continuous-wave (CW) ^{1}H heteronuclear decoupling was performed during the acquisition of ^{11}B NMR spectra at 50 kHz MAS. 100 kHz of SPINAL-64 ^{1}H heteronuclear decoupling was performed during the acquisition of ^{11}B NMR spectra at MAS frequencies of 25 kHz and below.[130] The symmetry-based $SR4_1^2$ heteronuclear dipolar recoupling sequences was applied on the ^{1}H channel (100 kHz at 50 kHz MAS) to reintroduce ^{1}H-^{11}B or ^{1}H-^{14}N dipolar couplings in the D-RINEPT and D-HMQC experiments, respectively.[93, 131-132] D-RINEPT and D-HMQC experiments were performed with previously described pulse sequences.[93, 132-135]

Dynamic Nuclear Polarization. DNP-enhanced SSNMR spectra were acquired on a 9.4 T 400 MHz/263 GHz Bruker solid-state NMR/gyrotron spectrometer equipped with an Avance III

console. All experiments were performed with a Bruker 3.2 mm DNP HXY probe at a sample temperature of a ca. 100 K and with an MAS frequency of 10 kHz. The *h*-BN and *h*-BNNS samples were prepared for DNP by impregnating 20.0 and 15.1 mg of sample with 17 μL and 14 μL of a 16 mM TEKPol tetrachloroethane (TCE) solution, respectively.[102] Both samples were packed into 3.2 mm sapphire DNP rotors with a Teflon insert and zirconia drive cap. To promote further DNP enhancements, both samples were degassed to remove dissolved oxygen. This was accomplished by initially freezing the sample at ca. 100 K and then allowing it to warm in the sample catcher for ca. 5 minutes, followed by re-freezing to ca. 100 K. The magnetic field strength was calibrated using ^{1}H chemical shifts referenced to neat tetramethylsilane with TCE ($\delta(^{1}H)$ = 6.2 ppm) as a secondary chemical shift reference. Previously reported relative NMR frequencies were used to indirectly reference ^{11}B and ^{15}N chemical shifts.[127] All DNP experiments were performed with a gyrotron cathode current of 160 mA. ^{1}H, ^{1}H→^{11}B CPMAS and direct excitation ^{11}B DNP enhancements were determined by performing NMR experiments with and without microwave irradiation and comparing the relative NMR signal intensities (Figure S8). ^{1}H, ^{15}N and low-power CT selective ^{11}B $\pi/2$ pulse lengths were 2.5 μs, 7.0 μs and 10.5 μs in duration. 100 kHz of ^{1}H heteronuclear decoupling was performed during the acquisition of ^{11}B and ^{15}N using the SPINAL-64 decoupling sequence.[130] ^{11}B spin-diffusion experiments were performed with previously described pulse sequences.[95, 136]

Density-Functional Theory Calculations. Periodic plane-wave DFT calculations were performed with the GIPAW approach[115] as used in CASTEP version 2017 R2.[126] Geometry optimizations and NMR calculations were performed using the Generalized Gradient Approximation with the exchange-correlation Perdew-Burke-Ernzerhof functional[137] (dispersion corrections were added using the Tkatchenko-Scheffler method[138]) and On-the-Fly ultrasoft Pseudopotential[139-140] with

zeroth-order regular approximation relativistic treatment.[141] A 630 eV kinetic energy cut-off and 0.07 $Å^{-1}$ k-point spacing was chosen for all calculations.

All structures were initially constructed from a previously reported crystal structure of *h*-BN consisting of two BN layers.[40] Zigzag and armchair edge terminations were obtained by building a super cell of the lattice and cleaving the crystal at h k l cleave planes of 0 -1 0 and 1 1 0, respectively. A 15 Å vacuum was applied to both the vertical and horizontal plane to represent an edge terminated environment for an isolated nanosheet consisting of two BN layers (Figure S13). Structures **1** and **2** had a net charge of zero while structure **3** had a net charge of –1 to account for the negatively charged four-coordinate boron species. All structures were geometry optimized and converged before performing the NMR calculations. Calculated chemical shielding values were converted to chemical shifts through a chemical shielding to chemical shift calibration plot constructed from previously reported compounds with known crystal structures and measured chemical shifts (Figure S12 and Table S4). The calculated ^{11}B C_Q and η were corrected to better match that observed experimental through a calibration plot (Figure S12 and Table S4).

Supporting Information:

The Supporting Information is available free of charge.

Additional TEM images, additional solid-state NMR spectra, solid-state NMR experimental parameters, DFT calibration plots, DFT calculated NMR parameters, and CIF files containing the atomic coordinates of the structural models.

Acknowledgements

Solid-state NMR spectroscopy and DFT-calculations (RWD and AJR), synthesis and DRIFT spectroscopy (TWG, PMH and WH), and electron microscopy (THK and LZ) were supported by the U.S. Department of Energy, Office of Science, Basic Energy Sciences, Materials Science and Engineering Division. We thank the Sensitive Instrument Facility of the Ames Laboratory for access to the electron microscopes. The Ames Laboratory is operated for the U.S. DOE by Iowa State University under Contract No. DE-AC02-07CH11358. We are grateful to Prof. Vincenzo Venditti (Iowa State University) for access to the tip sonicator used to exfoliate *h*-BN.

References

1. Novoselov, K. S.; Geim, A. K.; Morozov, S. V.; Jiang, D.; Zhang, Y.; Dubonos, S. V.; Grigorieva, I. V.; Firsov, A. A., Electric field effect in atomically thin carbon films. *Science* **2004,** *306* (5696), 666-669.
2. Geim, A. K.; Novoselov, K. S., The rise of graphene. *Nat. Mater.* **2007,** *6* (3), 183-191.
3. Stoller, M. D.; Park, S. J.; Zhu, Y. W.; An, J. H.; Ruoff, R. S., Graphene-Based Ultracapacitors. *Nano Lett.* **2008,** *8* (10), 3498-3502.
4. Castro Neto, A. H.; Guinea, F.; Peres, N. M. R.; Novoselov, K. S.; Geim, A. K., The electronic properties of graphene. *Rev. Mod. Phys.* **2009,** *81* (1), 109-162.
5. Geim, A. K., Graphene: Status and Prospects. *Science* **2009,** *324* (5934), 1530-1534.
6. Allen, M. J.; Tung, V. C.; Kaner, R. B., Honeycomb Carbon: A Review of Graphene. *Chem. Rev.* **2010,** *110* (1), 132-145.
7. Novoselov, K. S.; Jiang, D.; Schedin, F.; Booth, T. J.; Khotkevich, V. V.; Morozov, S. V.; Geim, A. K., Two-dimensional atomic crystals. *Proc. Natl. Acad. Sci. U. S. A.* **2005,** *102* (30), 10451-10453.
8. Golberg, D.; Bando, Y.; Huang, Y.; Terao, T.; Mitome, M.; Tang, C. C.; Zhi, C. Y., Boron Nitride Nanotubes and Nanosheets. *ACS Nano* **2010,** *4* (6), 2979-2993.
9. Lin, Y.; Williams, T. V.; Connell, J. W., Soluble, Exfoliated Hexagonal Boron Nitride Nanosheets. *J. Phys. Chem. Lett.* **2010,** *1* (1), 277-283.
10. Lin, Y.; Connell, J. W., Advances in 2D boron nitride nanostructures: nanosheets, nanoribbons, nanomeshes, and hybrids with graphene. *Nanoscale* **2012,** *4* (22), 6908-6939.
11. Butler, S. Z.; Hollen, S. M.; Cao, L. Y.; Cui, Y.; Gupta, J. A.; Gutierrez, H. R.; Heinz, T. F.; Hong, S. S.; Huang, J. X.; Ismach, A. F.; Johnston-Halperin, E.; Kuno, M.; Plashnitsa, V. V.; Robinson, R. D.; Ruoff, R. S.; Salahuddin, S.; Shan, J.; Shi, L.; Spencer, M. G.; Terrones, M.; Windl, W.; Goldberger, J. E., Progress, Challenges, and Opportunities in Two-Dimensional Materials Beyond Graphene. *ACS Nano* **2013,** *7* (4), 2898-2926.
12. Jiang, X.-F.; Weng, Q.; Wang, X.-B.; Li, X.; Zhang, J.; Golberg, D.; Bando, Y., Recent Progress on Fabrications and Applications of Boron Nitride Nanomaterials: A Review. *J. Mater. Sci. Technol.* **2015,** *31* (6), 589-598.
13. Zhang, K.; Feng, Y.; Wang, F.; Yang, Z.; Wang, J., Two dimensional hexagonal boron nitride (2D-hBN): synthesis, properties and applications. *J. Mater. Chem. C* **2017,** *5* (46), 11992-12022.
14. Yu, S.; Wang, X.; Pang, H.; Zhang, R.; Song, W.; Fu, D.; Hayat, T.; Wang, X., Boron nitride-based materials for the removal of pollutants from aqueous solutions: A review. *Chem. Eng. J.* **2018,** *333*, 343-360.
15. Shtansky, D. V.; Firestein, K. L.; Golberg, D. V., Fabrication and application of BN nanoparticles, nanosheets and their nanohybrids. *Nanoscale* **2018,** *10* (37), 17477-17493.
16. Tan, C. L.; Zhang, H., Two-dimensional transition metal dichalcogenide nanosheet-based composites. *Chem. Soc. Rev.* **2015,** *44* (9), 2713-2731.
17. Mannix, A. J.; Zhou, X.-F.; Kiraly, B.; Wood, J. D.; Alducin, D.; Myers, B. D.; Liu, X.; Fisher, B. L.; Santiago, U.; Guest, J. R.; Yacaman, M. J.; Ponce, A.; Oganov, A. R.; Hersam, M. C.; Guisinger, N. P., Synthesis of borophenes: Anisotropic, two-dimensional boron polymorphs. *Science* **2015,** *350* (6267), 1513.
18. Feng, B.; Zhang, J.; Zhong, Q.; Li, W.; Li, S.; Li, H.; Cheng, P.; Meng, S.; Chen, L.; Wu, K., Experimental realization of two-dimensional boron sheets. *Nat. Chem.* **2016,** *8*, 563.

19. Kambe, T.; Hosono, R.; Imaoka, S.; Kuzume, A.; Yamamoto, K., Solution Phase Mass Synthesis of 2D Atomic Layer with Hexagonal Boron Network. *J. Am. Chem. Soc.* **2019,** *141* (33), 12984-12988.
20. Nishino, H.; Fujita, T.; Cuong, N. T.; Tominaka, S.; Miyauchi, M.; Iimura, S.; Hirata, A.; Umezawa, N.; Okada, S.; Nishibori, E.; Fujino, A.; Fujimori, T.; Ito, S.-i.; Nakamura, J.; Hosono, H.; Kondo, T., Formation and Characterization of Hydrogen Boride Sheets Derived from MgB2 by Cation Exchange. *J. Am. Chem. Soc.* **2017,** *139* (39), 13761-13769.
21. Liu, H.; Neal, A. T.; Zhu, Z.; Luo, Z.; Xu, X.; Tománek, D.; Ye, P. D., Phosphorene: An Unexplored 2D Semiconductor with a High Hole Mobility. *ACS Nano* **2014,** *8* (4), 4033-4041.
22. Wei, Q.; Peng, X., Superior mechanical flexibility of phosphorene and few-layer black phosphorus. *Appl. Phys. Lett.* **2014,** *104* (25), 251915.
23. Yasaei, P.; Kumar, B.; Foroozan, T.; Wang, C.; Asadi, M.; Tuschel, D.; Indacochea, J. E.; Klie, R. F.; Salehi-Khojin, A., High-Quality Black Phosphorus Atomic Layers by Liquid-Phase Exfoliation. *Adv. Mater.* **2015,** *27* (11), 1887-1892.
24. Zhi, C.; Bando, Y.; Tang, C.; Kuwahara, H.; Golberg, D., Large-Scale Fabrication of Boron Nitride Nanosheets and Their Utilization in Polymeric Composites with Improved Thermal and Mechanical Properties. *Adv. Mater.* **2009,** *21* (28), 2889-2893.
25. Song, L.; Ci, L. J.; Lu, H.; Sorokin, P. B.; Jin, C. H.; Ni, J.; Kvashnin, A. G.; Kvashnin, D. G.; Lou, J.; Yakobson, B. I.; Ajayan, P. M., Large Scale Growth and Characterization of Atomic Hexagonal Boron Nitride Layers. *Nano Lett.* **2010,** *10* (8), 3209-3215.
26. Coleman, J. N.; Lotya, M.; O'Neill, A.; Bergin, S. D.; King, P. J.; Khan, U.; Young, K.; Gaucher, A.; De, S.; Smith, R. J.; Shvets, I. V.; Arora, S. K.; Stanton, G.; Kim, H. Y.; Lee, K.; Kim, G. T.; Duesberg, G. S.; Hallam, T.; Boland, J. J.; Wang, J. J.; Donegan, J. F.; Grunlan, J. C.; Moriarty, G.; Shmeliov, A.; Nicholls, R. J.; Perkins, J. M.; Grieveson, E. M.; Theuwissen, K.; McComb, D. W.; Nellist, P. D.; Nicolosi, V., Two-Dimensional Nanosheets Produced by Liquid Exfoliation of Layered Materials. *Science* **2011,** *331* (6017), 568-571.
27. Lin, Y.; Williams, T. V.; Xu, T. B.; Cao, W.; Elsayed-Ali, H. E.; Connell, J. W., Aqueous Dispersions of Few-Layered and Monolayered Hexagonal Boron Nitride Nanosheets from Sonication-Assisted Hydrolysis: Critical Role of Water. *J. Phys. Chem. C* **2011,** *115* (6), 2679-2685.
28. Li, L. H.; Cervenka, J.; Watanabe, K.; Taniguchi, T.; Chen, Y., Strong Oxidation Resistance of Atomically Thin Boron Nitride Nanosheets. *ACS Nano* **2014,** *8* (2), 1457-1462.
29. Blase, X.; Rubio, A.; Louie, S. G.; Cohen, M. L., Quasi-Particle Band-Structure of Bulk Hexagonal Boron-Nitride and Related Systems. *Phys. Rev. B* **1995,** *51* (11), 6868-6875.
30. Watanabe, K.; Taniguchi, T.; Kanda, H., Direct-bandgap properties and evidence for ultraviolet lasing of hexagonal boron nitride single crystal. *Nat. Mater.* **2004,** *3* (6), 404-409.
31. Grant, J. T.; Carrero, C. A.; Goeltl, F.; Venegas, J.; Mueller, P.; Burt, S. P.; Specht, S. E.; McDermott, W. P.; Chieregato, A.; Hermans, I., Selective oxidative dehydrogenation of propane to propene using boron nitride catalysts. *Science* **2016,** *354* (6319), 1570-1573.
32. Shi, L.; Wang, D. Q.; Song, W.; Shao, D.; Zhang, W. P.; Lu, A. H., Edge-hydroxylated Boron Nitride for Oxidative Dehydrogenation of Propane to Propylene. *ChemCatChem* **2017,** *9* (10), 1788-1793.
33. Huang, R.; Zhang, B. S.; Wang, J.; Wu, K. H.; Shi, W.; Zhang, Y. J.; Liu, Y. F.; Zheng, A. M.; Schlogl, R.; Su, D. S., Direct Insight into Ethane Oxidative Dehydrogenation over Boron Nitrides. *ChemCatChem* **2017,** *9* (17), 3293-3297.

34. Li, P.; Li, H. B.; Pan, X. L.; Tie, K.; Cui, T. T.; Ding, M. Z.; Bao, X. H., Catalytically Active Boron Nitride in Acetylene Hydrochlorination. *ACS Catal.* **2017,** *7* (12), 8572-8577.
35. Shi, L.; Wang, Y.; Yan, B.; Song, W.; Shao, D.; Lu, A. H., Progress in selective oxidative dehydrogenation of light alkanes to olefins promoted by boron nitride catalysts. *Chem. Commun.* **2018,** *54* (78), 10936-10946.
36. Chen, H.; Yang, Z.; Zhang, Z.; Chen, Z.; Chi, M.; Wang, S.; Fu, J.; Dai, S., Construction of a Nanoporous Highly Crystalline Hexagonal Boron Nitride from an Amorphous Precursor for Catalytic Dehydrogenation. *Angew. Chem., Int. Ed.* **2019,** *58* (31), 10626-10630.
37. Huang, C.; Chen, C.; Zhang, M.; Lin, L.; Ye, X.; Lin, S.; Antonietti, M.; Wang, X., Carbon-doped BN nanosheets for metal-free photoredox catalysis. *Nat. Commun.* **2015,** *6*, 7698.
38. Zheng, M.; Shi, J.; Yuan, T.; Wang, X., Metal-Free Dehydrogenation of N-Heterocycles by Ternary h-BCN Nanosheets with Visible Light. *Angew. Chem., Int. Ed.* **2018,** *57* (19), 5487-5491.
39. He, Z.; Kim, C.; Lin, L.; Jeon, T. H.; Lin, S.; Wang, X.; Choi, W., Formation of heterostructures via direct growth CN on h-BN porous nanosheets for metal-free photocatalysis. *Nano Energy* **2017,** *42*, 58-68.
40. Pease, R. S., Crystal Structure of Boron Nitride. *Nature* **1950,** *165* (4201), 722-723.
41. Park, C.-H.; Louie, S. G., Energy gaps and stark effect in boron nitride nanoribbons. *Nano Lett.* **2008,** *8* (8), 2200-2203.
42. Mukherjee, R.; Bhowmick, S., Edge Stabilities of Hexagonal Boron Nitride Nanoribbons: A First-Principles Study. *J. Chem. Theory Comput.* **2011,** *7* (3), 720-724.
43. Li, X.; Wu, X.; Zeng, X. C.; Yang, J., Band-Gap Engineering via Tailored Line Defects in Boron-Nitride Nanoribbons, Sheets, and Nanotubes. *ACS Nano* **2012,** *6* (5), 4104-4112.
44. Yamanaka, A.; Okada, S., Energetics and Electronic Structure of h-BN Nanoflakes. *Sci. Rep.* **2016,** *6*, 30653.
45. Alem, N.; Erni, R.; Kisielowski, C.; Rossell, M. D.; Gannett, W.; Zettl, A., Atomically thin hexagonal boron nitride probed by ultrahigh-resolution transmission electron microscopy. *Phys. Rev. B* **2009,** *80* (15).
46. Lopez-Bezanilla, A.; Huang, J. S.; Terrones, H.; Sumpter, B. G., Structure and Electronic Properties of Edge-Functionalized Armchair Boron Nitride Nanoribbons. *J. Phys. Chem. C* **2012,** *116* (29), 15675-15681.
47. Ding, Y.; Wang, Y.; Ni, J., The stabilities of boron nitride nanoribbons with different hydrogen-terminated edges. *Appl. Phys. Lett.* **2009,** *94* (23), 233107.
48. Krepel, D.; Hod, O., Effects of Edge Oxidation on the Structural, Electronic, and Magnetic Properties of Zigzag Boron Nitride Nanoribbons. *J. Chem. Theory Comput.* **2014,** *10* (1), 373-380.
49. Krepel, D.; Kalikhman-Razvozov, L.; Hod, O., Edge Chemistry Effects on the Structural, Electronic, and Electric Response Properties of Boron Nitride Quantum Dots. *J. Phys. Chem. C* **2014,** *118* (36), 21110-21118.
50. Li, L. L.; Yu, X. F.; Yang, X. J.; Zhang, X. H.; Xu, X. W.; Jin, P.; Zhao, J. L.; Wang, X. X.; Tang, C. C., Electronic properties and relative stabilities of heterogeneous edge-decorated zigzag boron nitride nanoribbons. *J. Alloys Compd.* **2015,** *649*, 1130-1135.
51. Zhao, R.; Gao, J.; Liu, Z.; Ding, F., The reconstructed edges of the hexagonal BN. *Nanoscale* **2015,** *7* (21), 9723-9730.
52. Yamanaka, A.; Okada, S., Polarity control of h-BN nanoribbon edges by strain and edge termination. *Phys. Chem. Chem. Phys.* **2017,** *19* (13), 9113-9117.

53. Maruyama, M.; Okada, S., Energetics and Electronic Structure of Triangular Hexagonal Boron Nitride Nanoflakes. *Sci. Rep.* **2018,** *8* (1), 16657-16657.
54. Kuang, W.; Hu, R.; Fan, Z. Q.; Zhang, Z. H., Strain-induced rich magnetic phase transitions and enhancement of magnetic stability for O-terminated h-BN nanoribbons. *J. Phys.: Condens. Matter* **2019,** *31* (14), 145301.
55. Gonçalves, J. A.; Batista, R. J. C.; Tromer, R.; Azevedo, S., Study of the stability and electronic properties of h-BN nanoribbons with reconstructed edges. *Chem. Phys. Lett.* **2019,** *727*, 126-132.
56. Arunachalam, V.; Vasudevan, S., Understanding Aqueous Dispersibility of Boron Nitride Nanosheets from H-1 Solid State NMR and Reactive Molecular Dynamics. *J. Phys. Chem. C* **2018,** *122* (8), 4662-4669.
57. Sideris, P. J.; Nielsen, U. G.; Gan, Z.; Grey, C. P., Mg/Al Ordering in Layered Double Hydroxides Revealed by Multinuclear NMR Spectroscopy. *Science* **2008,** *321* (5885), 113.
58. Brouwer, D. H.; Cadars, S.; Eckert, J.; Liu, Z.; Terasaki, O.; Chmelka, B. F., A General Protocol for Determining the Structures of Molecularly Ordered but Noncrystalline Silicate Frameworks. *J. Am. Chem. Soc.* **2013,** *135* (15), 5641-5655.
59. Harris, K. J.; Bugnet, M.; Naguib, M.; Barsoum, M. W.; Goward, G. R., Direct Measurement of Surface Termination Groups and Their Connectivity in the 2D MXene V2CTx Using NMR Spectroscopy. *J. Phys. Chem. C* **2015,** *119* (24), 13713-13720.
60. Hope, M. A.; Forse, A. C.; Griffith, K. J.; Lukatskaya, M. R.; Ghidiu, M.; Gogotsi, Y.; Grey, C. P., NMR reveals the surface functionalisation of Ti3C2 MXene. *Phys. Chem. Chem. Phys.* **2016,** *18* (7), 5099-5102.
61. Wang, Y.; Yang, B.; Wan, B.; Xi, X.; Zeng, Z.; Liu, E.; Wu, G.; Liu, Z.; Wang, W., Degradation of black phosphorus: a real-time31P NMR study. *2D Mater.* **2016,** *3* (3), 035025.
62. Paul, G.; Bisio, C.; Braschi, I.; Cossi, M.; Gatti, G.; Gianotti, E.; Marchese, L., Combined solid-state NMR, FT-IR and computational studies on layered and porous materials. *Chem. Soc. Rev.* **2018,** *47* (15), 5684-5739.
63. Martini, F.; Borsacchi, S.; Barcaro, G.; Caporali, M.; Vanni, M.; Serrano-Ruiz, M.; Geppi, M.; Peruzzini, M.; Calucci, L., Phosphorene and Black Phosphorus: The 31P NMR View. *J. Phys. Chem. Lett.* **2019,** *10* (17), 5122-5127.
64. Cai, W.; Piner, R. D.; Stadermann, F. J.; Park, S.; Shaibat, M. A.; Ishii, Y.; Yang, D.; Velamakanni, A.; An, S. J.; Stoller, M.; An, J.; Chen, D.; Ruoff, R. S., Synthesis and Solid-State NMR Structural Characterization of ^{13}c-Labeled Graphite Oxide. *Science* **2008,** *321* (5897), 1815-1817.
65. Pines, A.; Gibby, M. G.; Waugh, J. S., Proton-enhanced NMR of dilute spins in solids. *J. Chem. Phys.* **1973,** *59* (2), 569-590.
66. Sindorf, D. W.; Maciel, G. E., Cross-polarization magic-angle-spinning silicon-29 nuclear magnetic resonance study of silica gel using trimethylsilane bonding as a probe of surface geometry and reactivity. *J. Phys. Chem.* **1982,** *86* (26), 5208-5219.
67. Morris, H. D.; Ellis, P. D., Aluminum-27 cross polarization of aluminas. The NMR spectroscopy of surface aluminum atoms. *J. Am. Chem. Soc.* **1989,** *111* (16), 6045-6049.
68. Lesage, A.; Lelli, M.; Gajan, D.; Caporini, M. A.; Vitzthum, V.; Miéville, P.; Alauzun, J.; Roussey, A.; Thieuleux, C.; Mehdi, A.; Bodenhausen, G.; Coperet, C.; Emsley, L., Surface Enhanced NMR Spectroscopy by Dynamic Nuclear Polarization. *J. Am. Chem. Soc.* **2010,** *132* (44), 15459-15461.

69. Piveteau, L.; Ong, T.-C.; Rossini, A. J.; Emsley, L.; Copéret, C.; Kovalenko, M. V., Structure of Colloidal Quantum Dots from Dynamic Nuclear Polarization Surface Enhanced NMR Spectroscopy. *J. Am. Chem. Soc.* **2015,** *137* (43), 13964-13971.
70. Oatley, C. W.; Nixon, W. C.; Pease, R. F. W., Scanning Electron Microscopy. In *Adv. Electron. Electron Phys.*, Marton, L., Ed. Academic Press: 1966; Vol. 21, pp 181-247.
71. Wang, Z. L., Transmission Electron Microscopy of Shape-Controlled Nanocrystals and Their Assemblies. *J. Phys. Chem. B* **2000,** *104* (6), 1153-1175.
72. Warner, J. H.; Rümmeli, M. H.; Bachmatiuk, A.; Büchner, B., Atomic Resolution Imaging and Topography of Boron Nitride Sheets Produced by Chemical Exfoliation. *ACS Nano* **2010,** *4* (3), 1299-1304.
73. Tan, C. L.; Cao, X. H.; Wu, X. J.; He, Q. Y.; Yang, J.; Zhang, X.; Chen, J. Z.; Zhao, W.; Han, S. K.; Nam, G. H.; Sindoro, M.; Zhang, H., Recent Advances in Ultrathin Two-Dimensional Nanomaterials. *Chem. Rev.* **2017,** *117* (9), 6225-6331.
74. Colthup, N. B., Spectra-Structure Correlations in the Infra-Red Region. *J. Opt. Soc. Am.* **1950,** *40* (6), 397-400.
75. Ogden, J. S.; Young, N. A., The characterisation of molecular boric acid by mass spectrometry and matrix isolation infrared spectroscopy. *J. Chem. Soc., Dalton Trans.* **1988,** (6), 1645-1652.
76. Peak, D.; Luther, G. W.; Sparks, D. L., ATR-FTIR spectroscopic studies of boric acid adsorption on hydrous ferric oxide. *Geochim. Cosmochim. Acta* **2003,** *67* (14), 2551-2560.
77. Kentgens, A. P. M., A practical guide to solid-state NMR of half-integer quadrupolar nuclei with some applications to disordered systems. *Geoderma* **1997,** *80* (3), 271-306.
78. Ashbrook, S. E.; Duer, M. J., Structural information from quadrupolar nuclei in solid state NMR. *Concepts Magn. Reson., Part A* **2006,** *28A* (3), 183-248.
79. Angel Wong, Y.-T.; Bryce, D. L., Chapter Four - Recent Advances in 11B Solid-State Nuclear Magnetic Resonance Spectroscopy of Crystalline Solids. In *Annu. Rep. NMR Spectrosc.*, Webb, G. A., Ed. Academic Press: 2018; Vol. 93, pp 213-279.
80. Brus, J.; Czernek, J.; Urbanova, M.; Kobera, L.; Jegorov, A., An efficient 2D 11B–11B solid-state NMR spectroscopy strategy for monitoring covalent self-assembly of boronic acid-derived compounds: the transformation and unique architecture of bortezomib molecules in the solid state. *Phys. Chem. Chem. Phys.* **2017,** *19* (1), 487-495.
81. Marchetti, P. S.; Kwon, D.; Schmidt, W. R.; Interrante, L. V.; Maciel, G. E., High-field boron-11 magic-angle spinning NMR characterization of boron nitrides. *Chem. Mater.* **1991,** *3* (3), 482-486.
82. Kanehashi, K.; Saito, K., Structural analysis of boron compounds using 11B-3QMAS solid state NMR. *J. Mol. Struct.* **2002,** *602-603*, 105-113.
83. Love, A. M.; Thomas, B.; Specht, S. E.; Hanrahan, M. P.; Venegas, J. M.; Burt, S. P.; Grant, J. T.; Cendejas, M. C.; McDermott, W. P.; Rossini, A. J.; Hermans, I., Probing the Transformation of Boron Nitride Catalysts under Oxidative Dehydrogenation Conditions. *J. Am. Chem. Soc.* **2019,** *141* (1), 182-190.
84. Jin, C.; Lin, F.; Suenaga, K.; Iijima, S., Fabrication of a Freestanding Boron Nitride Single Layer and Its Defect Assignments. *Phys. Rev. Lett.* **2009,** *102* (19), 195505.
85. Meyer, J. C.; Chuvilin, A.; Algara-Siller, G.; Biskupek, J.; Kaiser, U., Selective Sputtering and Atomic Resolution Imaging of Atomically Thin Boron Nitride Membranes. *Nano Lett.* **2009,** *9* (7), 2683-2689.

86. Suenaga, K.; Kobayashi, H.; Koshino, M., Core-Level Spectroscopy of Point Defects in Single Layer h-BN. *Phys. Rev. Lett.* **2012,** *108* (7), 075501.
87. Liao, Y.; Tu, K.; Han, X.; Hu, L.; Connell, J. W.; Chen, Z.; Lin, Y., Oxidative Etching of Hexagonal Boron Nitride Toward Nanosheets with Defined Edges and Holes. *Sci. Rep.* **2015,** *5*, 14510.
88. Ryu, G. H.; Park, H. J.; Ryou, J.; Park, J.; Lee, J.; Kim, G.; Shin, H. S.; Bielawski, C. W.; Ruoff, R. S.; Hong, S.; Lee, Z., Atomic-scale dynamics of triangular hole growth in monolayer hexagonal boron nitride under electron irradiation. *Nanoscale* **2015,** *7* (24), 10600-10605.
89. Kroeker, S.; Stebbins, J. F., Three-Coordinated Boron-11 Chemical Shifts in Borates. *Inorg. Chem.* **2001,** *40* (24), 6239-6246.
90. Turner, G. L.; Smith, K. A.; Kirkpatrick, R. J.; Oldfield, E., Boron-11 nuclear magnetic resonance spectroscopic study of borate and borosilicate minerals and a borosilicate glass. *J. Magn. Reson.* **1986,** *67* (3), 544-550.
91. Neumair, S. C.; Vanicek, S.; Kaindl, R.; Többens, D. M.; Martineau, C.; Taulelle, F.; Senker, J.; Huppertz, H., HP-KB3O5 Highlights the Structural Diversity of Borates: Corner-Sharing BO3/BO4 Groups in Combination with Edge-Sharing BO4 Tetrahedra. *Eur. J. Inorg. Chem.* **2011,** *2011* (27), 4147-4152.
92. Hansen, M. R.; Vosegaard, T.; Jakobsen, H. J.; Skibsted, J., 11B Chemical Shift Anisotropies in Borates from 11B MAS, MQMAS, and Single-Crystal NMR Spectroscopy. *J. Phys. Chem. A* **2004,** *108* (4), 586-594.
93. Trebosc, J.; Hu, B.; Amoureux, J. P.; Gan, Z., Through-space R3-HETCOR experiments between spin-1/2 and half-integer quadrupolar nuclei in solid-state NMR. *J. Magn. Reson.* **2007,** *186* (2), 220-227.
94. Venkatesh, A.; Hanrahan, M. P.; Rossini, A. J., Proton detection of MAS solid-state NMR spectra of half-integer quadrupolar nuclei. *Solid State Nucl. Magn. Reson.* **2017,** *84*, 171-181.
95. Edén, M.; Frydman, L., Homonuclear NMR Correlations between Half-Integer Quadrupolar Nuclei Undergoing Magic-Angle Spinning. *J. Phys. Chem. B* **2003,** *107* (51), 14598-14611.
96. Linder, M.; Henrichs, P. M.; Hewitt, J. M.; Massa, D. J., Use of carbon–carbon nuclear spin diffusion for the study of the miscibility of polymer blends. *J. Chem. Phys.* **1985,** *82* (3), 1585-1598.
97. Perras, F. A.; Korobkov, I.; Bryce, D. L., NMR crystallography of sodium diphosphates: combining dipolar, shielding, quadrupolar, diffraction, and computational information. *CrystEngComm* **2013,** *15* (43), 8727-8738.
98. Lelli, M.; Gajan, D.; Lesage, A.; Caporini, M. A.; Vitzthum, V.; Miéville, P.; Héroguel, F.; Rascón, F.; Roussey, A.; Thieuleux, C.; Boualleg, M.; Veyre, L.; Bodenhausen, G.; Coperet, C.; Emsley, L., Fast Characterization of Functionalized Silica Materials by Silicon-29 Surface-Enhanced NMR Spectroscopy Using Dynamic Nuclear Polarization. *J. Am. Chem. Soc.* **2011,** *133* (7), 2104-2107.
99. Vitzthum, V.; Miéville, P.; Carnevale, D.; Caporini, M. A.; Gajan, D.; Copéret, C.; Lelli, M.; Zagdoun, A.; Rossini, A. J.; Lesage, A.; Emsley, L.; Bodenhausen, G., Dynamic nuclear polarization of quadrupolar nuclei using cross polarization from protons: surface-enhanced aluminium-27 NMR. *Chem. Commun.* **2012,** *48* (14), 1988-1990.

100. Rossini, A. J.; Zagdoun, A.; Lelli, M.; Lesage, A.; Copéret, C.; Emsley, L., Dynamic Nuclear Polarization Surface Enhanced NMR Spectroscopy. *Acc. Chem. Res.* **2013,** *46* (9), 1942-1951.
101. Valla, M.; Rossini, A. J.; Caillot, M.; Chizallet, C.; Raybaud, P.; Digne, M.; Chaumonnot, A.; Lesage, A.; Emsley, L.; van Bokhoven, J. A.; Copéret, C., Atomic Description of the Interface between Silica and Alumina in Aluminosilicates through Dynamic Nuclear Polarization Surface-Enhanced NMR Spectroscopy and First-Principles Calculations. *J. Am. Chem. Soc.* **2015,** *137* (33), 10710-10719.
102. Zagdoun, A.; Rossini, A. J.; Gajan, D.; Bourdolle, A.; Ouari, O.; Rosay, M.; Maas, W. E.; Tordo, P.; Lelli, M.; Emsley, L.; Lesage, A.; Copéret, C., Non-aqueous solvents for DNP surface enhanced NMR spectroscopy. *Chem. Commun.* **2012,** *48* (5), 654-656.
103. Hanrahan, M. P.; Chen, Y.; Blome-Fernández, R.; Stein, J. L.; Pach, G. F.; Adamson, M. A. S.; Neale, N. R.; Cossairt, B. M.; Vela, J.; Rossini, A. J., Probing the Surface Structure of Semiconductor Nanoparticles by DNP SENS with Dielectric Support Materials. *J. Am. Chem. Soc.* **2019,** *141* (39), 15532-15546.
104. Bak, M.; Rasmussen, J. T.; Nielsen, N. C., SIMPSON: A General Simulation Program for Solid-State NMR Spectroscopy. *J. Magn. Reson.* **2000,** *147* (2), 296-330.
105. Jeschke, G.; Jansen, M., High-Resolution 14N Solid-State NMR Spectroscopy. *Angew. Chem., Int. Ed.* **1998,** *37* (9), 1282-1283.
106. Jeschke, G.; Hoffbauer, W.; Jansen, M., A comprehensive NMR study of cubic and hexagonal boron nitride. *Solid State Nucl. Magn. Reson.* **1998,** *12* (1), 1-7.
107. Gervais, C.; Babonneau, F., High resolution solid state NMR investigation of various boron nitride preceramic polymers. *J. Organomet. Chem.* **2002,** *657* (1), 75-82.
108. Gervais, C.; Maquet, J.; Babonneau, F.; Duriez, C.; Framery, E.; Vaultier, M.; Florian, P.; Massiot, D., Chemically Derived BN Ceramics: Extensive 11B and 15N Solid-State NMR Study of a Preceramic Polyborazilene. *Chem. Mater.* **2001,** *13* (5), 1700-1707.
109. Toury, B.; Gervais, C.; Dibandjo, P.; Cornu, D.; Miele, P.; Babonneau, F., High-resolution 15N solid-state NMR investigations on borazine-based precursors. *Appl. Organomet. Chem.* **2004,** *18* (5), 227-232.
110. Gervais, C.; Framery, E.; Duriez, C.; Maquet, J.; Vaultier, M.; Babonneau, F., 11B and 15N solid state NMR investigation of a boron nitride preceramic polymer prepared by ammonolysis of borazine. *J. Eur. Ceram. Soc.* **2005,** *25* (2), 129-135.
111. Gastreich, M.; Marian, C. M., Ab initio prediction of 15N-NMR chemical shift in α-boron nitride based on an analysis of connectivities. *J. Comput. Chem.* **1998,** *19* (7), 716-725.
112. Cavadini, S.; Antonijevic, S.; Lupulescu, A.; Bodenhausen, G., Indirect detection of nitrogen-14 in solids via protons by nuclear magnetic resonance spectroscopy. *J. Magn. Reson.* **2006,** *182* (1), 168-172.
113. Cavadini, S., Indirect detection of nitrogen-14 in solid-state NMR spectroscopy. *Prog. Nucl. Magn. Reson. Spectrosc.* **2010,** *56* (1), 46-77.
114. Nishiyama, Y.; Endo, Y.; Nemoto, T.; Utsumi, H.; Yamauchi, K.; Hioka, K.; Asakura, T., Very fast magic angle spinning 1H-14N 2D solid-state NMR: Sub-micro-liter sample data collection in a few minutes. *J. Magn. Reson.* **2011,** *208* (1), 44-48.
115. Pickard, C. J.; Mauri, F., All-electron magnetic response with pseudopotentials: NMR chemical shifts. *Phys. Rev. B* **2001,** *63* (24), 245101.
116. Yates, J. R.; Pham, T. N.; Pickard, C. J.; Mauri, F.; Amado, A. M.; Gil, A. M.; Brown, S. P., An Investigation of Weak CH⋯O Hydrogen Bonds in Maltose Anomers by a Combination of

Calculation and Experimental Solid-State NMR Spectroscopy. *J. Am. Chem. Soc.* **2005,** *127* (29), 10216-10220.
117. Charpentier, T., The PAW/GIPAW approach for computing NMR parameters: A new dimension added to NMR study of solids. *Solid State Nucl. Magn. Reson.* **2011,** *40* (1), 1-20.
118. Bonhomme, C.; Gervais, C.; Babonneau, F.; Coelho, C.; Pourpoint, F.; Azaïs, T.; Ashbrook, S. E.; Griffin, J. M.; Yates, J. R.; Mauri, F.; Pickard, C. J., First-Principles Calculation of NMR Parameters Using the Gauge Including Projector Augmented Wave Method: A Chemist's Point of View. *Chem. Rev.* **2012,** *112* (11), 5733-5779.
119. Ferrara, C.; Tealdi, C.; Pedone, A.; Menziani, M. C.; Rossini, A. J.; Pintacuda, G.; Mustarelli, P., Local versus Average Structure in LaSrAl3O7: A NMR and DFT Investigation. *J. Phys. Chem. C* **2013,** *117* (45), 23451-23458.
120. Franco, F.; Baricco, M.; Chierotti, M. R.; Gobetto, R.; Nervi, C., Coupling Solid-State NMR with GIPAW ab Initio Calculations in Metal Hydrides and Borohydrides. *J. Phys. Chem. C* **2013,** *117* (19), 9991-9998.
121. Njegic, B.; Levin, E. M.; Schmidt-Rohr, K., 125Te NMR chemical-shift trends in PbTe–GeTe and PbTe–SnTe alloys. *Solid State Nucl. Magn. Reson.* **2013,** *55-56*, 79-83.
122. de Souza, F. A. L.; Ambrozio, A. R.; Souza, E. S.; Cipriano, D. F.; Scopel, W. L.; Freitas, J. C. C., NMR Spectral Parameters in Graphene, Graphite, and Related Materials: Ab Initio Calculations and Experimental Results. *J. Phys. Chem. C* **2016,** *120* (48), 27707-27716.
123. Namespetra, A. M.; Hirsh, D. A.; Hildebrand, M. P.; Sandre, A. R.; Hamaed, H.; Rawson, J. M.; Schurko, R. W., 35Cl solid-state NMR spectroscopy of HCl pharmaceuticals and their polymorphs in bulk and dosage forms. *CrystEngComm* **2016,** *18* (33), 6213-6232.
124. Veinberg, S. L.; Friedl, Z. W.; Lindquist, A. W.; Kispal, B.; Harris, K. J.; O'Dell, L. A.; Schurko, R. W., 14N Solid-State NMR Spectroscopy of Amino Acids. *ChemPhysChem* **2016,** *17* (23), 4011-4027.
125. Carnahan, S. L.; Lampkin, B. J.; Naik, P.; Hanrahan, M. P.; Slowing, I. I.; VanVeller, B.; Wu, G.; Rossini, A. J., Probing O–H Bonding through Proton Detected 1H–17O Double Resonance Solid-State NMR Spectroscopy. *J. Am. Chem. Soc.* **2019,** *141* (1), 441-450.
126. Clark Stewart, J.; Segall Matthew, D.; Pickard Chris, J.; Hasnip Phil, J.; Probert Matt, I. J.; Refson, K.; Payne Mike, C., First principles methods using CASTEP. In *Z. Kristallogr. - Cryst. Mater.*, 2005; Vol. 220, p 567.
127. Harris, R. K.; Becker, E. D.; Cabral de Menezes, S. M.; Goodfellow, R.; Granger, P., NMR Nomenclature: Nuclear Spin Properties and Conventions for Chemical Shifts: IUPAC Recommendations 2001. *Solid State Nucl. Magn. Reson.* **2002,** *22* (4), 458-483.
128. Yao, Z.; Kwak, H.-T.; Sakellariou, D.; Emsley, L.; Grandinetti, P. J., Sensitivity enhancement of the central transition NMR signal of quadrupolar nuclei under magic-angle spinning. *Chem. Phys. Lett.* **2000,** *327* (1), 85-90.
129. Prasad, S.; Kwak, H.-T.; Clark, T.; Grandinetti, P. J., A Simple Technique for Determining Nuclear Quadrupole Coupling Constants with RAPT Solid-State NMR Spectroscopy. *J. Am. Chem. Soc.* **2002,** *124* (18), 4964-4965.
130. Fung, B. M.; Khitrin, A. K.; Ermolaev, K., An Improved Broadband Decoupling Sequence for Liquid Crystals and Solids. *J. Magn. Reson.* **2000,** *142* (1), 97-101.
131. Brinkmann, A.; Kentgens, A. P. M., Proton-Selective 17O−H Distance Measurements in Fast Magic-Angle-Spinning Solid-State NMR Spectroscopy for the Determination of Hydrogen Bond Lengths. *J. Am. Chem. Soc.* **2006,** *128* (46), 14758-14759.

132. Hu, B.; Trébosc, J.; Amoureux, J. P., Comparison of several hetero-nuclear dipolar recoupling NMR methods to be used in MAS HMQC/HSQC. *J. Magn. Reson.* **2008,** *192* (1), 112-122.
133. Lafon, O.; Wang, Q.; Hu, B.; Vasconcelos, F.; Trébosc, J.; Cristol, S.; Deng, F.; Amoureux, J.-P., Indirect Detection via Spin-1/2 Nuclei in Solid State NMR Spectroscopy: Application to the Observation of Proximities between Protons and Quadrupolar Nuclei. *J. Phys. Chem. A* **2009,** *113* (46), 12864-12878.
134. Cavadini, S.; Vitzthum, V.; Ulzega, S.; Abraham, A.; Bodenhausen, G., Line-narrowing in proton-detected nitrogen-14 NMR. *J. Magn. Reson.* **2010,** *202* (1), 57-63.
135. Shen, M.; Trébosc, J.; Lafon, O.; Pourpoint, F.; Hu, B.; Chen, Q.; Amoureux, J. P., Improving the resolution in proton-detected through-space heteronuclear multiple quantum correlation NMR spectroscopy. *J. Magn. Reson.* **2014,** *245*, 38-49.
136. Jeener, J.; Meier, B. H.; Bachmann, P.; Ernst, R. R., Investigation of exchange processes by two-dimensional NMR spectroscopy. *J. Chem. Phys.* **1979,** *71* (11), 4546-4553.
137. Perdew, J. P.; Burke, K.; Ernzerhof, M., Generalized Gradient Approximation Made Simple. *Phys. Rev. Lett.* **1996,** *77* (18), 3865-3868.
138. Tkatchenko, A.; Scheffler, M., Accurate Molecular Van Der Waals Interactions from Ground-State Electron Density and Free-Atom Reference Data. *Phys. Rev. Lett.* **2009,** *102* (7), 073005.
139. Vanderbilt, D., Soft self-consistent pseudopotentials in a generalized eigenvalue formalism. *Phys. Rev. B* **1990,** *41* (11), 7892-7895.
140. Yates, J. R.; Pickard, C. J.; Mauri, F., Calculation of NMR chemical shifts for extended systems using ultrasoft pseudopotentials. *Phys. Rev. B* **2007,** *76* (2), 024401.
141. Green, T. F. G.; Yates, J. R., Relativistic nuclear magnetic resonance J-coupling with ultrasoft pseudopotentials and the zeroth-order regular approximation. *J. Chem. Phys.* **2014,** *140* (23), 234106.